Title

Design, Construction, and Performance of the Electromagnetic Module of the D0 End Calorimeter

Journal

Nuclear Instruments and Methods in Physics Research A, 325(3)

Authors

Aihara, H.
Arthur, A.A.
Dahl, O.I.
et al.

Publication Date

1992-07-01

LBL-31378
UC-414
Preprint

Lawrence Berkeley Laboratory
UNIVERSITY OF CALIFORNIA

Physics Division

Submitted to Nuclear Instruments and Methods in Physics Research A

DESIGN, CONSTRUCTION, AND PERFORMANCE OF THE ELECTROMAGNETIC MODULE OF THE DØ END CALORIMETER

DØ Collaboration

July 1992

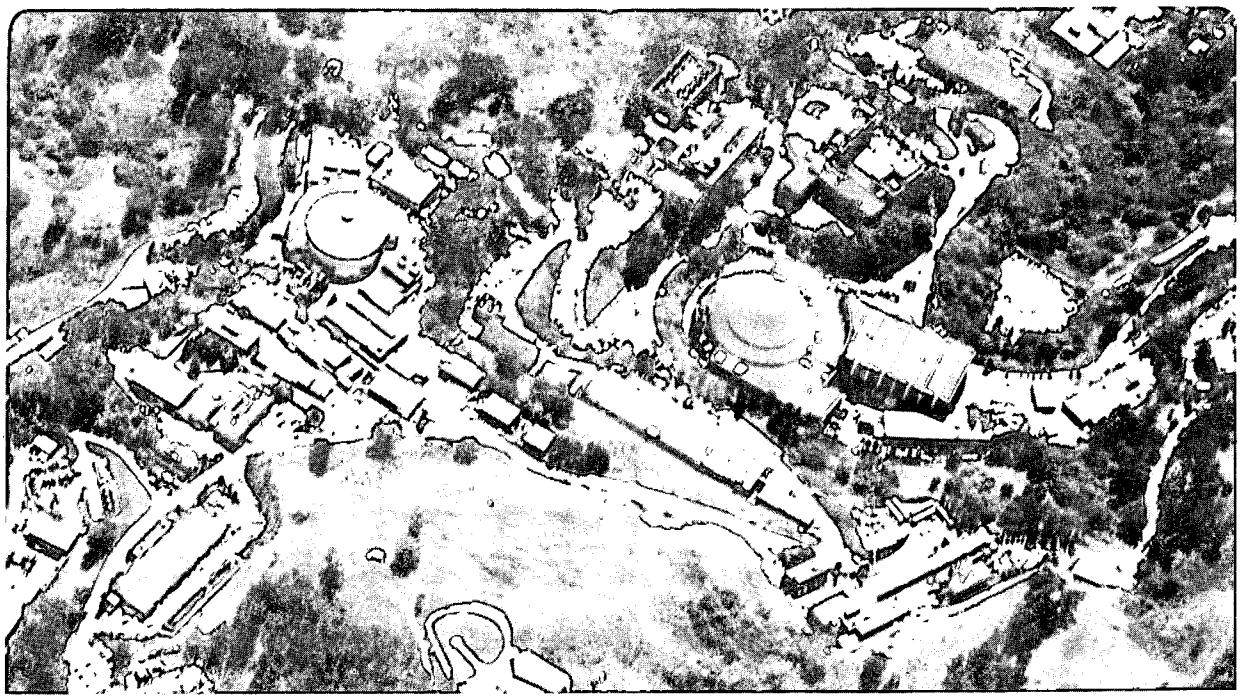

Prepared for the U.S. Department of Energy under Contract Number DE-AC03-76SF00098

DISCLAIMER

LBL-31378
D0 Note 1448

Design, Construction, and Performance of the Electromagnetic Module of the DØ End Calorimeter

H. Aihara, A.A. Arthur, O.I. Dahl, P.H. Eberhard, W.R. Edwards, R.L. Fulton, J.M. Haughian, R.J. Madaras, N.A. Roe, D.B. Shuman, A.L. Spadafora, M.L. Stevenson, J.D. Taylor and W.A. Wenzel

Lawrence Berkeley Laboratory,[a] University of California, Berkeley, California 94720

J. Chen, C. Cretsinger,[b] G. E. Forden, A. Milder, J. Rutherfoord and M. Shupe

University of Arizona, Tucson, Arizona 85721

S.H.Aronson, J. Featherly, B. G. Gibbard, H. A. Gordon, J. M. Guida, W. Guryn, S. Kahn and S. Protopopescu

Brookhaven National Laboratory, Upton, New York 11973

D. Cutts, D. Nešić and J. S. Hoftun

Brown University, Providence, Rhode Island 02912

P. Franzini[c] and P. M. Tuts

Columbia University, New York, New York 10027

N. Amos, F. Bartlett, P. Bhat, J. H. Christenson, W. E. Cooper, R. Dixon, H. E. Fisk, S. Fuess, N. Graf, H. Haggerty, A. S. Ito, A. Jonckheere, B. Klima, R. Lipton, W. Merritt, H. Prosper, A. Peryshkin, R. Raja, R. P. Smith, D. Stewart and M. Tartaglia

Fermi National Accelerator Laboratory, Batavia, Illinois 60510

[a]This work was supported by the Director, Office of Energy Research, Office of High Energy and Nuclear Physics, High Energy Physics Division, of the U.S. Department of Energy under Contract No. DE-AC03-76SF00098

[b]Present address: University of Rochester, Rochester, New York 14627

[c]Present address: Lab. Nazionali di Frascati dell'INFN, I-00044 Frascati, Italy

A.P. White[d] and Z. Wolf[e]

University of Florida, Gainesville, Florida 32611

R. Avellaneda, W. Dharmaratna, M. Goforth, R. Madden, H. Piekarz, H. D. Wahl, J. Womersley and J. Xu

Florida State University, Tallahassee, Florida 32306

N. Hadley, D. Norman and K. Streets

University of Maryland, College Park, Maryland 20742

K. De and H. Neal

University of Michigan, Ann Arbor, Michigan 48109

M. Abolins, D. Edmunds, D. P. Owen, B. Pi, H. Weerts and Y. Xia

Michigan State University, East Lansing, Michigan 48824

J. Kotcher, J. Kourlas, P. Nemethy, J. Sculli and Q. Zhu

New York University, New York, New York 10003

G. C. Blazey, J. Borders, P. Draper,[d] S. Durston, T. Ferbel, R. Hirosky and F. Lobkowicz

University of Rochester, Rochester, New York 14627

M. Demarteau, P. D. Grannis, J. A. Guida, W. Karsh, M. Marx, L. Rasmussen and R.D. Schamberger

State University of New York, Stony Brook, New York 11794

July 1992

[d]Present address: University of Texas at Arlington, Arlington, Texas 76019
[e]Present address: SSC Laboratory, Dallas, Texas

Abstract

The two End Calorimeter Electromagnetic (ECEM) modules of the DØ liquid argon calorimeter system have been constructed as monolithic units of 1 m radius to provide full azimuthal coverage in the forward and backward regions ($1.4 < |\eta| < 4.0$) for the study of $p\bar{p}$ collisions at the Fermilab Tevatron Collider. An ECEM module consists of 18 layers of absorber disks (mostly 4 mm thick uranium) with interleaved signal disks that have readout pads in semi-projective towers. The mechanical design and construction of the ECEM modules is described in detail. The performance of one ECEM module has been studied in beam tests with electrons. Results are given for the linearity and uniformity of response, the energy and position resolutions, and pion rejection.

1 Introduction

This article describes the construction and test beam measurements of the DØ End Calorimeter Electromagnetic (ECEM) modules. These two modules are part of the uranium liquid argon calorimeter system of the DØ detector[1, 2], one of two large multipurpose experiments at the Tevatron Proton-Antiproton Collider at the Fermi National Accelerator Laboratory.

The primary design goal of the DØ detector is the precision study of high mass, large transverse momentum phenomena with particular emphasis on measurements of leptons (electrons and muons), photons, jets (clusters of produced particles), and missing transverse momentum indicative of penetrating particles (such as neutrinos). To accomplish these goals, the detector design stresses uniform, hermetic, and precise measurement of localized energy deposition with calorimeters which cover essentially the whole solid angle.

In the DØ calorimeters, uranium plates are used as the absorber medium. The use of uranium helps to equalize the calorimeter response to electrons and hadrons. This is important for minimizing the fluctuations in the observed energies of jets, whose particle content may vary. In addition, the high density of uranium leads to a compact calorimeter design.

Liquid argon is used in the DØ calorimeters as the active ionization medium because of its ease of calibration, its stability and uniformity of response, and its radiation hardness. This choice also makes it possible to measure the energy of showering particles with very fine spatial segmentation.

The DØ calorimeter system consists of a cylindrical Central Calorimeter and two End Calorimeters covering angles down to within 1° of the beamline (Fig. 1). Each of the three calorimeters contains an electromagnetic section with thin (3 or

4 mm) uranium plates, a fine hadronic section with thick (6 mm) uranium plates, and a coarse hadronic section with very thick (46 mm) copper or stainless-steel plates. Printed circuit boards with segmented detection pads are interleaved between the absorber plates to detect the ionization in the liquid argon. All of the DØ calorimeter modules use a uniform technology to facilitate the relative calibration between modules. The calorimeters are designed with minimal cracks and other uninstrumented regions in order to provide essentially hermetic coverage.

In the following sections the design and construction of the electromagnetic modules of the DØ End Calorimeters will be discussed in detail. The ECEM modules were constructed at LBL and one of the two (their construction is identical) was studied in a test beam at Fermilab. The results obtained using electron test beams are presented here; the analysis of the combined response of the electromagnetic and hadronic End Calorimeter modules to pion beams is given in Reference[3].

2 The Electromagnetic Module

2.1 General Description

The ECEM module, shown schematically in Fig. 2, provides full azimuthal (ϕ) coverage for the precise energy and position measurement of electrons and photons in the forward and backward regions ($1.4 < |\eta| < 4.0$)[†]. In order to minimize energy losses in radial cracks and other uninstrumented areas, the electromagnetic module is built as a monolithic unit of alternating disks of signal boards and uranium absorber plates. The module has a total thickness of 24.1 cm, a diameter of approximately 2 meters, and a weight of approximately 5 tons. In the DØ detector, it is positioned with its front face 1.70 m from the nominal interaction point.

The mechanical design, which is described in Section 2.4, employs a stainless-steel strongback and an aluminum central tube to support the uranium plates and the signal disks. There are 96 titanium tie-rods (4.8 mm diameter) that penetrate the module to maintain the spacing of the liquid argon gaps.

The signal disks (see Section 2.2) are constructed from five-layer printed circuit boards laminated with facesheets coated with a high resistivity epoxy (see Fig. 3). The resistive coat is maintained at positive high voltage to provide the drift field; any ionization charge drifting in the gap induces a signal on the pads.

[†] η is the pseudorapidity defined as $\eta = -\ln\tan(\theta/2)$, where θ is the polar angle from the beam axis.

The uranium disks (see Section 2.3) are made by joining three 4 mm thick uranium plates (approximately 60 cm wide by 2 m long) side by side at their edges. The plate thickness of 4 mm was the minimum needed to keep such large plates flat during the rolling process.

The basic sampling cell of the ECEM module, shown in Fig. 3, consists of a 4 mm depleted-uranium absorber plate, a 2.3 mm liquid argon gap, a 4.3 mm NEMA G-10 multilayer printed circuit signal board, and another 2.3 mm liquid argon gap. The module contains 18 sampling cells in depth, for a total of 20.1 radiation lengths (X_0) of material (calculated at normal incidence).

The first two cells have 1.4 mm thick stainless-steel absorber disks instead of uranium, to form "low mass" gaps to monitor the energy loss in front of the ECEM in the approximately 2.3 X_0 of material in the steel cryostat walls and tracking chambers.

In the eleventh cell the 2 cm thick stainless-steel strongback replaces the uranium absorber plate. In a GEANT Monte Carlo calculation using 100 GeV electrons it was found that the sampling fraction ($E_{\rm LAr}/E_{\rm total}$) for this cell was lower than that of a uranium cell at that longitudinal depth. To compensate for this we substituted a thin (1.4 mm) stainless-steel disk for the absorber in the following cell so that the average sampling fraction of these two cells would be approximately equal to that of the uranium cells. As can be seen from the test beam results given in Section 3, this design gives a linear energy response from 10 to 150 GeV and good energy resolution with a very small constant term.

Signals from the 18 cells are ganged into four separate longitudinal depth sections (referred to below as EM1, EM2, EM3, and EM4) that consist of 2, 2, 6 and 8 cells, with thicknesses of 0.3, 2.6, 7.9, and 9.3 X_0, respectively. This longitudinal segmentation provides information about the development of the electromagnetic shower and is valuable in distinguishing electrons from charged pions. The design of EM1 and EM2 as 2-cell sections was made to provide fine sampling in the front part of the calorimeter in order to statistically distinguish single photons from π^0's by the conversion probability in the first few radiation lengths.

Transverse segmentation is provided by the copper readout pads (Fig. 4) on the signal boards, each covering an η,ϕ interval of $\Delta\eta \times \Delta\phi = 0.1 \times \pi/32(\approx 0.1)$. In the third longitudinal section (EM3), which typically contains 65% of the electromagnetic shower energy, the transverse segmentation is doubled in both directions to 0.05×0.05 in order to provide better shower position resolution. However, at high

η values, this segmentation would require pads that are smaller than the Molière radius, which for this detector is approximately 1 cm. Using this value to set the minimum pad size, a segmentation of 0.1×0.1 (i.e. the value used in the other sections of the calorimeter) is used in EM3 for $\eta > 2.6$. The pad sizes† in this third section range from $13 \times 13\,\mathrm{mm}^2$ to $52 \times 52\,\mathrm{mm}^2$. The highest η region of the module ($3.2 \leq |\eta| \leq 4.1$) is beyond the tracking coverage of the forward drift chamber and is divided into three η towers of roughly equal physical size.

The segmented pads are arranged in a semi-projective tower geometry which continues from the ECEM into the hadronic modules behind it. The semi-projective tower geometry differs from true projective geometry in that the pad radial boundaries do not increase successively for each of the 18 cells, but increase in groups of 2 for the first 10 cells, and in groups of 4 cells thereafter. This simplifies the fabrication of the multilayer signal boards by reducing the number of different types required in the stack.

Table 1 summarizes the module parameters. The following sections will describe in detail the design and construction of the ECEM module.

2.2 Signal Readout Disks

The cross section of the multilayer boards used in the construction of the signal disks can be seen in Fig. 3. These five-layer printed circuit boards have segmented copper pads on the outer surfaces connected via plated-through holes to radial traces (0.5 mm wide) on the innermost layer. There are shielding ground layers between the pads and the traces that run beneath them, which reduce the signal cross-talk to a negligible level.

Using the largest multilayer boards that were practical to fabricate[4], our design employed 22.5° wedges with radii up to about 1 meter (see Table 1). The artwork layout of these boards was required to provide stay-clear zones for the tie-rods (see Section 2.4) that penetrate the module. By flipping over every other board in a disk, the requisite eight-fold pattern of stay-clear zones was obtained with a minimal number of artwork designs. The traces were laid out so that the boards have the same readout sequence whether flipped over or not. An additional design constraint was that adjacent traces went to adjacent pads so as to minimize the error in the measurement of transverse momentum that would result from any residual cross-talk.

† If R is the radial distance of a pad from the beam axis, the radial span of a pad, for a specified $\Delta\eta$, is given by: $|\Delta R| = R\Delta\eta/\tanh\eta$.

The use of long radial leads and internal ground planes results in an increase of the cell capacitance. The major contributions to the net capacitance are from the pads to ground planes, pads to absorbers, and leads to ground planes. Fig. 5 shows the measured capacitance of the EM3 section of the calorimeter towers (six ganged cells), as a function of radial distance from the beam axis, at a constant azimuth. The calculated values for the pad and lead contributions given in the figure show that leads dominate the total capacitance for the small pads at small radius. The range of capacitance values in each of the longitudinal sections is given in Table 1. The coaxial readout cables that go from the module to the cryostat feedthrough add an additional 0.5 - 1.8 nF, depending on the cable length.

Before a multilayer board was used in a disk assembly it was first subjected to a series of quality assurance tests. These included a check of the board's outline, measurements of its thickness at ten locations (mean thickness of 3.07 mm with an rms deviation of 0.01 mm), a complete test for pad shorts or opens, and finally a capacitance measurement of each channel.

The robustness of these multilayer boards under cryocycling was established by a series of tests with liquid nitrogen[†] in which no damage to plated-through holes, traces, or pads was observed. Finally, to avoid the use of material that would poison the liquid argon of the calorimeter, these boards were fabricated solely from copper, NEMA G-10 (without flame-retardant), and its b-stage epoxy.

Facesheets of 0.5 mm thick NEMA G-10 screen-printed with a thin coating of high resistivity carbon loaded epoxy[5] are laminated onto both sides of the multilayer boards to provide the positive high voltage electrode of the calorimeter cells as shown in Fig. 3. This coated facesheet replaces the conventional blocking capacitor, so that both signal pads and absorber disks can be held at ground potential. The normal operating voltage is +2.5 kV, corresponding to a drift field of 11 kV/cm. The connection to the coating is made via a 1 mm copper trace that runs around the perimeter of the disk under the resistive coat. Using the largest sheets of G-10 available, the facesheet for a disk was made by joining together two semicircular pieces. The surface resistivity of the coating is approximately 40 MΩ per square at room temperature and increases by about a factor of two when cooled to liquid argon temperature.

The assembly of the multilayer boards into signal disks proceeded in the following steps. First, 16 tested multilayer boards were positioned in a fixture to form a

[†]The boiling point of nitrogen is 77 K versus 87 K for argon.

disk and epoxy was drawn into narrow radial gaps between the boards to butt-join them together. The copper pads were then cleaned with Scotch-Brite abrasive in preparation for lamination of the circular facesheets onto each side of the disk. This lamination was performed using a large steel rolling pin to evenly spread a room-temperature curing epoxy. After both sides had been laminated, the assembled disk was mounted on a numerically controlled milling machine and holes were drilled through the disk at the locations of the tie-rods. The resistive coat was then cut back by 3 mm around these holes (and at the outer radius) in order to isolate the high voltage. Finally, connectors (headers) were soldered at the outer radius of the disk. The inspection of the finished disk included high voltage testing and a capacitance measurement.

2.3 Uranium Absorber Plates

The 4 mm thick absorber plates for the calorimeter were fabricated from depleted-uranium billets[6]. This included hot-rolling the billets into plates, shearing to rough size, thermal annealing, flattening using rollers, shearing to finished dimensions, and hole punching. Sharp edges were rounded and burrs were removed with a belt sander. Liquid honing removed salts and oxides left over from earlier steps. Frequently, this uncovered surface flaws which were then ground away with a hand grinder. The majority of these ground-out surface flaws were less than 0.1 mm deep, although many extended over lengths of more than 10 cm.

The thermal contraction of rolled uranium plate is normally quite anisotropic: in cooling from room to liquid argon temperature the thermal contraction in the direction perpendicular to the rolling direction is about twice that along the rolling direction. It was found, however, that if the uranium plates are vacuum annealed at 800°C, the thermal contraction in the two directions is equal to within 10% (and approximately equal to that of stainless steel). This uniformity greatly simplifies the design of the thermal contraction clearances in the module's structural elements. Moreover, annealing helped achieve the required plate flatness, and so all the ECEM uranium plates were vacuum annealed.

The spacing between the tie-rods (see Section 2.4) that serve to position and flatten the uranium plates was determined by studies on 4 mm thick full size (60 cm by 200 cm) plates at both room and liquid argon temperatures. It was found that with a spacing of approximately 30 cm between tie-rods the deflection of the uranium plates was kept to less than 0.5 mm at all points. The placement of these rods, whose

number was kept to a minimum, was arranged in the eight-fold symmetric pattern shown in Fig. 6.

A known problem in using bare uranium in detector construction is the formation of oxide layers which, if thick enough, tend to shed loose oxide particles thereby raising radiation and toxicity concerns. The dark oxide which forms on the plates after rolling is quite tenacious and does not cause problems. However, areas that required grinding, or regions where water remained in extended contact with the uranium develop a different oxide (yellow/green in color) which did not adhere well. It is known that trapped water accelerates oxidation, while the presence of gaseous oxygen has a retarding effect[7]. To remove the loose uranium oxide from the surface of the uranium, the ECEM plates were cleaned at Fermilab using a process that consisted of scouring with Scotch-Brite and washing with jets of hot water under high pressure. By keeping the plates in a controlled, dry atmosphere during the module construction, shipping, and testing, development of the loose oxide was minimized.

At the end of the fabrication process, each uranium plate was inspected and checked on a template. Each plate was required to be within all dimensional specifications including thickness (within $\pm$ 0.25 mm of average), flatness (less than $\pm$ 0.5 mm over a 25 cm span, as measured between tie-rod holes), hole location (within $\pm$ 0.8 mm of nominal), hole diameter (within $\pm$ 0.08 mm of nominal), and straightness of edges (true to $\pm$ 0.25 mm over the full length).

Disks of uranium were assembled by joining a central plate to D-shaped side plates, as shown in Fig. 6. Small stainless-steel links, which are fastened to the uranium with roll-pins, are used to hold the uranium together. The link design produces a 1 mm gap between the central and side plates. This gap has very little effect on the energy response of the calorimeter (see the test beam studies of the affected region as discussed in Section 3.8).

In order to provide a robust grounding connection to the uranium, niobium pins were percussion-welded to the uranium plates at the outer radius.

Using a computer-controlled ultrasonic probe with an accuracy of $\pm$ 50 μm, the thickness of all uranium plates and also of all signal disks was measured prior to stacking. Measurements were taken at points on a 10 cm $\times$ 10 cm grid. The thickness distributions for the uranium plates and signal disks are shown in Fig. 7. The mean thickness of the uranium plates is 3.97 mm with an rms deviation of 0.09 mm; the mean thickness of the signal disks is 4.31 mm with an rms deviation of 0.06 mm.

2.4 Structural Elements

The structural elements of the ECEM module were designed to withstand assembly, handling, transportation, installation, and cooldown loads, with an acceptable safety factor, but minimal impact on the detector's performance. As can be seen in the module cross section in Fig. 8, the design distributes the weight of the uranium plates and the signal disks onto a central aluminum tube, which in turn is supported by a stainless-steel strongback. Four brackets at the outer edge of the strongback are used to mount the ECEM module onto the front of the ECMH (End Calorimeter Middle Hadronic) modules. These brackets were designed to support and position the ECEM module using a minimum of space and allowing for differential thermal contraction rates between modules.

The strongback is a 2.3 m diameter, 2 cm thick stainless-steel plate that serves as the first absorber layer in the EM4 section of the module. A finite-element analysis study established that this thickness is adequate to withstand the normal gravitational load, as well as the worst-case anticipated load during transportation (3 g). The strongback plate, which was machined in a single operation on a numerically controlled milling machine, provides a flat reference surface for the module assembly, and precisely locates the central support tube and the tie-rods that penetrate the module.

A central aluminum tube supports the absorber plates and the signal disks, and positions them in the transverse dimension. Aluminum was chosen to minimize the mass of dead material in front of the hadronic modules. Based on a finite-element analysis, this 11.4 cm diameter tube, with a wall thickness of 9.5 mm, should have a maximum sag of no more than 0.2 mm at the ends of the tube.

Penetrating the module at the locations shown in Fig. 6, are titanium tie-rods that serve to maintain the argon gap thickness and the flatness of the absorber plates. A tie-rod assembly, shown in Fig. 9, consists of a 4.8 mm diameter titanium threaded rod with both titanium and nylon spacers. Titanium was chosen for the 96 bolts to provide sufficient strength with minimum mass of dead material. These tie-rods constrain the absorber plates and signal disks longitudinally, but not transversely, in order to allow for differential thermal contraction between the various components. Our design goal was to maintain all the liquid argon gaps at the nominal thickness of 2.3 mm by appropriately shimming the tie-rod spacers (and similar spacers at the central support tube), based on the thickness map (see Fig. 7) of the plates and disks. Interpolating between the points of the measurement grid, the thickness of

the argon gaps has been calculated for each longitudinal section of each tower of the module. The distribution of the calculated mean thickness of the argon gaps for all towers is shown in Fig. 10. The mean thickness is 2.28 mm and the rms deviation is 0.03 mm. The response of the calorimeter in the vicinity of these bolts has been studied in the test beam, and the results are discussed in Section 3.8.

2.5 Module Assembly

The two ECEM modules were assembled in a horizontal position, beginning with the insertion of the central support tube and the tie-rods into the strongback. The signal and absorber disks were then placed over these, using a manually operated vacuum lifting fixture. The azimuthal orientation of each disk was fixed by a keyed slot in the disk, and the longitudinal location established using spacers and shims at the tie-rods (Section 2.4) and at the central support tube. The EM4 longitudinal section was stacked first and then, after the assembly was flipped over, the remaining sections were stacked. The completed stack was compressed by nuts on the tie-rods and at the central support tube, and the stack height was measured with respect to the strongback surface at eight locations. All deviations were kept to within 0.3% of the nominal value, in agreement with the value estimated from the thickness measurements of uranium plates, signal disks, spacers and shims.

After stacking, kapton flex circuits[8] that gang together the corresponding pads within a longitudinal depth section were installed. Terminated with pin-socket connectors for mating to the signal disks, these flex circuits proved to be very reliable in cryocycling tests.

Low inductance ground buses of corrugated copper-beryllium were installed at 32 locations around the perimeter of the module. These connect the absorber plates and the internal shielding layers of the signal disks. On the signal disks, soldered ground straps connect the 16 multilayer boards to ensure good azimuthal grounding.

A total of 26 platinum resistor temperature devices (RTD's) were attached to the module at both ends of the central support tube (2), at the strongback perimeter (4), at the stainless-steel surfaces of EM1 (4) and EM4 (8), at the outer radius of an EM3 signal disk (4), and at the outer radius of an EM4 signal disk (4). The temperature sensors are used during the cooldown and warmup of the module to check that the maximum temperature gradient allowed in the design of the module's structural elements (50°C between any two sensors) is not exceeded.

The module assembly was then completed by mounting perforated fiber-epoxy

covers that serve to protect the flex circuits but do not impede the flow of liquid argon.

Fig. 11 shows a completed ECEM module mounted onto the hadronic modules in the DØ End Calorimeter.

2.6 Module Testing

As the calorimeter module was assembled, a high voltage test was performed on each layer to check that there were no shorts in the gap between the signal disk and the adjacent uranium plate. For this test, a voltage of +3 kV was applied across the gaps. The currents were usually monitored overnight with a chart recorder. A quiescent current of < 100 nA was required for each surface to pass inspection. Occasionally, higher currents were caused by metal burrs, G-10 fibers, or bits of lint; these were removed using adhesive-tipped insulating strips, or by disassembling and vacuuming, or by applying higher voltage to burn out the object.

After each longitudinal section was fully assembled, the capacitance of each read-out channel in that section was measured by injecting a known charge and reading back the induced voltage, thereby determining the capacitance C. The capacitance test was used primarily to verify that all of the longitudinally ganged signal pads in a tower were connected. The accuracy of the capacitance measurement was approximately $0.01 \times C$, with a constant term of the order of a few pF. This was adequate for detecting the absence of a single pad in any tower.

In addition, a resistance test was performed to verify that all pads were isolated from each other and from ground. In the first module to be constructed, several inter-pad shorts were found through this test. These shorts had resistances ranging from several ohms to several hundred kΩ. In tests performed on spare multilayer boards, such resistive shorts were found to be caused by copper dust, generated when the pads were cleaned with Scotch-Brite prior to the lamination of the facesheet. The copper dust was trapped in the glue joints when the facesheets were laminated; however, these concentrations were not sufficient to cause shorts. Resistive shorts were, in fact, generated during high voltage testing of pads that were not properly grounded through grounding plugs. This caused induced charge to accumulate on the pad, then to discharge across the glue joint, and thereby form a resistive path between pads. Several boards with resistive shorts were subsequently replaced in the first module, and more effective cleaning procedures, as well as more care with the insertion of grounding plugs, prevented any further occurrence of this problem.

Finally, before shipment to Fermilab, the ECEM module for each End Calorimeter was tested at the construction site at LBL in a cold tub filled with liquid argon. The cold test was performed with the module in the vertical position, corresponding to its orientation in the DØ detector. The module was first cooled down using N_2 gas at the rate of 4°C/hr. The cool-down was monitored with the temperature sensors (RTD's) located on the module, and the rate was regulated so that the maximum temperature difference between sensors did not exceed 50°C. When the module was cold, the tub was filled with liquid argon. No shorts were observed in either module when high voltage was applied. In the testing of the first ECEM module, the initial current draw was 90-120 nA per side at +3 kV, corresponding to 3.6 pA/cm^2, consistent with the expected current due to uranium-induced ionization in the liquid argon. The current draw then increased exponentially, reaching a maximum in 8–10 hours of 300–800 nA/side (corresponding to $\sim$ 10–30 pA/cm^2), then decreased with a much longer time constant of several days. We have no satisfactory explanation for this behaviour[9]. Moreover, the second module did not exhibit this anomalous current draw. Based on our three months of operation of the first module in the test beam (described in Sec. 3) we have no reason to believe that this anomalous current draw will have any noticeable effect on the calorimeter's performance.

A capacitance test was also performed on the cold module to verify continuity of signal. A failure rate of 0.04% was observed in the first module and was attributed to bad contacts induced by thermal cycling of the ganging circuits. Some of the pins on these connectors were later observed to have whitish deposits which were thought to have originated when the solder flux was cleaned with alcohol. A more thorough cleaning procedure was instituted for all connectors, and in the cold test of the second module no failures were observed.

The completed and tested modules were shipped to Fermilab by air-ride truck. A support fixture was attached to each module at four points around the circumference and at its center. This assembly was housed in a shipping container, which was engineered to isolate the module from shocks and vibrations. The calorimeter was mounted horizontally inside a wooden crate that was placed in an outer crate lined with blocks of polyethylene foam. Bags of desiccant were packed inside the crate to maintain low humidity. The shipping container was outfitted with heaters to prevent the foam from stiffening at low temperatures. The largest accelerations measured on the module (0.5 g vertical and 0.4 g horizontal) were much smaller than the allowed accelerations ($\pm$3.0 g vertical and $\pm$2.0 g horizontal). No adverse effect was observed

as a result of the five day trip from Berkeley to FNAL.

3 Performance in the Test Beam

3.1 Experimental Configuration

The DØ ECEM and ECIH (End Calorimeter Inner Hadronic) modules were studied in a test beam at the Neutrino-West beamline of Fermilab prior to their installation at the collider. These modules were configured (Fig. 12) as in the DØ End Calorimeter. An ECMH (End Calorimeter Middle Hadronic) module was located behind the ECIH to monitor leakage of hadronic showers, but this information was not used in the analysis presented here (See Ref. [3]).

The material inside the cryostat upstream of the ECEM module was designed to approximate the distribution of material at DØ . A liquid argon excluder, located in front of the ECEM module, was constructed of Rohacell slabs. It contained a 2.5 cm thick stainless-steel plate (to simulate the cryostat wall of the DØ End Calorimeter) and a 4.4 cm thick aluminum plate at small angles (to simulate the material due to the end plates of the DØ vertex chamber). The test beam cryostat had a thin window consisting of two 1.6 mm steel plates in the region illuminated by the beam. An estimate of the total amount of material upstream of the front face of the ECEM module derived from our Monte Carlo simulation (Sec. 3.3) is shown in Fig. 13.

The cryostat rested on a computer controlled transporter that oriented the module so that the beam could strike it along projective towers, as with the incident particles at the collider. The transporter made it possible to study the calorimeter response over the full range in η subtended by the module (1.4 to 4.0), and over $\pm 15°$ in azimuthal angle. In addition, different vertex positions, ranging from -30 to 30 cm relative to the virtual interaction point, could be selected.

Scintillators in the beamline provided the trigger, and PWC's, located before and after the final bending magnet, were used to measure particle momenta and trajectories. Pions and electrons were available for study, with momenta ranging from 10 to 150 GeV/c, and with typical momentum spreads of 1.1% (measured to an accuracy of 0.2%). The beam spot was about 1 x 2 cm^2. Cherenkov counters were used for particle identification.

The calorimeters were instrumented with the full DØ electronic readout system in the active region illuminated by the beam. In the surrounding border region groups of channels were ganged together and read out. This allowed the energy flow out of

the central region to be monitored, while keeping the total channel count low (there was a total of 1452 channels). The DØ readout electronics is described in detail elsewhere[10, 11]. For this test, the coaxial readout cables were of the same length as those used in the DØ calorimeter. These low impedance (30Ω) coaxial cables are used within the cryostat to carry signals to the multilayer feedthrough boards which reorder the signals so that all signals in a particular tower are adjacent to each other. The outputs from the charge-sensitive preamplifiers, mounted on the cryostat, are connected to the shaping and sampling hybrid circuits by twisted-pair cables. The shaped signals are sampled twice at an interval of 2.2 μs by a BaseLine Subtractor (BLS). The resulting signals are multiplexed (16 signals to 1 line), double-buffered to reduce dead time, and transmitted to ADCs through $\times 1$ or $\times 8$ switchable amplifiers, which provide 15-bit equivalent dynamic range using 12-bit ADCs. The ADCs reside in a VME crate, and a backplane VME bus is used to read the ADC outputs into a VME buffer, which in turn sends the data to the dual-port memories of a set of Micro VAX-II computers. One ADC crate digitizes 4608 calorimeter signals in approximately 160 μs.

3.2 Data Analysis

The analysis of the data proceeds by first correcting individual channels for the electronic pedestals and gains which were measured once per eight hours and once per day, respectively. The data were taken without threshold suppression of channels; channels containing signals within one standard deviation of their pedestal value were ignored (unless stated otherwise). The linearity of the gains was studied using a high precision pulser with different attenuator settings[12]. Over a range of attenuator settings corresponding to 2.5 to 50 GeV, the deviations from linearity for all channels were found to be less than 0.25%. The channel-to-channel relative response for a given pulser amplitude had an rms spread of $\sim 2.3\%$. The gains were corrected offline for their dependence on the temperature (0.08%/°C) of the BLS and preamplifier crates.

The energy of electromagnetic showers was reconstructed by summing the ADC counts in the four longitudinal sections of the ECEM and the first section of the ECIH. (The first longitudinal section, IH1, of the ECIH module has 16 cells with 6 mm uranium plates for a total thickness of 30 X_0). Relative sampling fractions for each longitudinal section were determined from the data (see Sec. 3.5). The small pad-to-pad corrections to the sampling fractions, calculated from the measured

component thicknesses (see Sec. 2.3), did not improve our results and therefore were not used in the following analysis.

The signals are summed in an $n \times n$ array of 0.1×0.1 semi-projective towers. The array size needed to contain an electromagnetic shower varies with η, corresponding to the geometrical dependence of pad size on η. In a Monte Carlo study of 100 GeV electrons (Sec. 3.3), it was found that 99.6% containment is achieved by summing an array of 5×5 towers at $\eta = 1.95$; at $\eta = 2.55$, an array of 9×9 towers is needed for the same lateral containment.

3.3 Monte Carlo Simulation

As part of the analysis of testbeam data, a detailed Monte Carlo study of the ECEM response to electrons was performed. The testbeam geometry was modeled using the GEANT (version 3.14) framework[13]. Monte Carlo simulations were performed to establish a benchmark for comparison with the data.

The Monte Carlo geometry includes the testbeam cryostat and the liquid argon excluder, as well as beamline elements such as PWC's and scintillators located downstream of the momentum analyzing dipole magnet. The ECEM was modeled as a series of uranium plates and liquid argon gaps, with signal boards represented by layers of copper laminate and G-10. Each uranium plate was given a unique thickness corresponding to the average of the measured value for that plate, as determined from the grid of measurements made during assembly. Features such as the titanium bolts which function as tie rods and the small gaps between the three sections which comprise a uranium disk were modeled for the studies described in Sec. 3.8. For all of the simulations described here, the energy cutoffs employed in GEANT were 1 MeV for both electrons and photons; Molière scattering and delta-ray production were part of the simulation. Electronic noise and noise due to the uranium activity were not included in the results shown here.

3.4 Operation of the Module

The ECEM module was operated at +2.5 kV during the test beam run. Immediately after the high voltage was applied, anomalous current draw was observed, similar to that found in the post-construction cold test (Section 2.6). Within about ten days, all the currents dropped to the values expected from uranium radioactivity-induced ionization, with the exception of one disk surface, which had about twice the average current for the duration of the run.

The pulse height as a function of high voltage (HV) for 100 GeV electrons, at a "benchmark" tower ($\eta = 1.95$), is shown in Fig. 14. In the vicinity of the operating voltage of 2.5 kV (11 kV/cm) the slope of the response is approximately 0.002%/Volt. The curve shown in Fig. 14 is a fit to the form[14]:

$$Q = Q_0 f \frac{s}{d}[1 - e^{-d/s}] \tag{1}$$

where Q is the collected charge, f is the fraction of electrons that do not recombine with positive ions, d is the width of the liquid argon gap (0.23 cm), and s is the electron mean free path (in cm) related to the field E (in kV/cm) and effective oxygen content p (in ppm O_2) by $s = 0.12E/p$. For the recombination factor we use a linear dependence on the electric field:

$$Q_0 f = C_1 E + C_2 \tag{2}$$

The free parameters in the fit are C_1, C_2, and p. The value of p obtained from the fit in Fig. 14 is 0.487 ± 0.004 ppm (statistical error only). Such HV scans were repeated approximately every ten days, and a very small increase in p was found during the course of the run, consistent with the results discussed below.

In order to detect any change in the calorimeter response with time, the signal for 100 GeV electrons was measured during the run at the $\eta = 1.95$ benchmark tower, essentially on a daily basis. A plot of the mean pulse height versus time (days into the run) is shown in Fig. 15 for the runs taken after the temperature monitoring of the electronics crates was implemented. The linear fit shown in Fig. 15 is:

$$\mu = A(1 + bt) \tag{3}$$

where μ is the mean pulse height and t is time. The rate of decrease of signal with time obtained is $b = (-0.12 \pm 0.04)\%/40$ days. If we assume this decrease in signal is entirely due to increased effective oxygen contamination, this would correspond to an increase of the oxygen content of $\Delta p = 0.013$ ppm over the 40 days, assuming the above stated value for p. This small increase in p is consistent with the upper limit of the increase in oxygen contamination estimated from measurements of α and β cell argon purity monitors[15].

The noise observed in the calorimeter arises from both the preamp noise, which is proportional to the channel capacitance, and uranium radioactivity-induced noise, which is proportional to the area of the pad. Fig. 16 shows the pedestal distribution for a single summed tower (all EM plus IH1 sections - eight electronics channels

in total) at the $\eta = 1.95$ benchmark. For this tower, the pedestal rms ($\sigma_{\rm ped}$) is 12.6 ADC counts, which corresponds to 47 MeV of electromagnetic energy. With the high voltage off, there is only electronics noise; in this case the pedestal rms decreases to 9 ADC counts.

Muons comprised approximately 3% of the hadron beam, and a muon trigger was set up using scintillation counters downstream of the cryostat and counters downstream of an additional 3 m of steel shielding. The pulse height spectrum for 15 GeV muons is shown in Fig. 17 for separate longitudinal sections, and in Fig. 18 for all ECEM longitudinal sections combined. This study was performed with the beam directed at the $\eta = 1.95$ benchmark tower, and only the signals from this tower (i.e. a 1×1 array) are included in these pulse height distributions. A muon peak can be observed above the pedestal in all longitudinal sections of the calorimeter. The distributions are fit with the Moyal function[16] (an approximate analytic expression for the Landau distribution) convoluted with a Gaussian resolution function to determine the most probable value (MPV). The signal to noise ratio, given by MPV/$\sigma_{\rm ped}$, is: 3.7±0.3, 4.2±0.3, 5.1±0.4, and 8.3±0.4 for the four individual layers; it is 10.7±0.6 for the combined ECEM signal (IH1 layer not included). More information regarding the muon response can be found in Ref. [3].

3.5 Linearity and Energy Resolution

A series of runs was taken at the $\eta = 1.95$ benchmark position with electron beams of momenta ranging from 10 to 150 GeV/c to study the calorimeter linearity and energy resolution. For this analysis, events were required to have a track reconstructed by the PWC system and the measured momentum was used to correct on an event-by-event basis for the spread in the beam momentum. The particle was required to be flagged as an electron by the Cherenkov counters.

As described in Sec. 3.2, the calorimeter signals were summed for the four ECEM longitudinal sections and the first hadronic section (IH1) in an array of 5×5 towers about the tower with the maximum signal. As an illustration of the longitudinal shower profile, the mean fraction of the total signal in each section (calculated using a 3σ pedestal suppression) is tabulated in Table 2 for 50 GeV electrons. The fractions obtained from the Monte Carlo simulation are also listed and agree very well with the data. Approximately 65% of the energy is contained in the EM3 layer. The fraction observed in the IH1 layer is about 0.4%.

The measured energy (in GeV) for event i is calculated as:

$$E_i = \alpha \sum_{j=1}^{5} \beta_j ADC_{ji} + \delta \tag{4}$$

where β_j is the weight, or relative inverse sampling fraction, given to the ADC counts in each readout layer. The third layer weight, β_3, is set equal to 1, and α is an overall scale factor. The additive term, δ, is to allow for energy loss before the calorimeter and is determined from the data. The ratios of the inverse sampling fractions for each layer, as calculated from the dE/dX values for minimum ionizing particles (see Table 3), can be used as the layer weights in Eq. 4. An improved set of weights can be obtained from the data by minimizing the deviation of the reconstructed energy from the track momentum measured by the PWC system, i.e. minimizing:

$$\chi^2 = \sum_{k=1}^{7} \sum_{i=1}^{N_k} \frac{(p_i - E_i)^2}{\sigma_i^2} \tag{5}$$

where p_i is the measured track momentum for event i. The first sum is over the seven runs with beam momenta ranging from 10 to 150 GeV/c, and the second sum is over the N_k events of a run with a given momentum setting. An equal number of events (1000) at each momentum setting is used to obtain weights which are optimized uniformly over the momentum range. The estimated measurement error, σ_i, used in calculating the χ^2 is taken from a fit to the resolution, which is discussed below.

The optimized layer weights (β_j) given in Table 3 are consistent with the ratios calculated from minimum ionizing dE/dX losses, except for the first layer. In effect, the slightly smaller optimized weight obtained for this layer corresponds to a dE/dX value calculated with the upstream iron plate taken at 75% of its nominal thickness in computing the layer's dead material. This minimization procedure was also performed on sets of electrons generated with the GEANT Monte Carlo (Sec. 3.3) and the resulting layer weights are given in the last column of Table 3.

The distribution of reconstructed energy for different beam momenta is shown in Fig. 19. Comparing the mean from a Gaussian fit to the measured energy distribution with the mean track momentum for each beam momentum setting (Fig. 20a), we find that the response of the calorimeter is linear to within $\pm 0.3\%$ over the momentum range studied. Using the optimized layer weights of Table 3, the scale factor, α, is $(3.74 \pm 0.01) \times 10^{-3}$ GeV/ADC and the offset, δ, is 0.30 ± 0.02 GeV. A non-zero (but somewhat smaller) value for the offset was also found using the Monte Carlo electrons ($\delta = 0.20 \pm 0.02$ GeV).

The fractional energy resolution, calculated as σ/E, where σ and E are the standard deviation and mean from the Gaussian fits, is shown in Fig. 20b. We assume the energy dependence of the resolution to be of the quadratic form:

$$\left(\frac{\sigma}{E}\right)^2 = C^2 + \frac{S^2}{P} + \frac{N^2}{P^2} \tag{6}$$

where P is the beam momentum in GeV/c, C is a constant contribution from systematic errors such as remaining channel-to-channel variations in gain, S is due to the statistical error in sampling, and N represents energy independent contributions to σ such as electronic and uranium noise. The results of the fit are given in Table 4. The noise term in the fit to the data ($N = 0.29 \pm 0.03$ Gev) is consistent with the value obtained from the pedestal widths for an array of 5×5 towers. (Noise was not included in the Monte Carlo simulation.)

Energy scans were also taken at $\eta = 2.10$ and at $\eta = 2.55$ so that we could study the response of the module in locations with different amounts of upstream material (See Fig. 13). The design of the steel plate that simulated the DØ cryostat walls included a hole at $\eta = 2.10$ in order to provide a location where we could study the response in the absence of this material. The data taken with the beam directed through this hole were analyzed using the set of energy independent layer weights (β_j) derived from the $\eta = 1.95$ data, but the slope (α) and offset (δ) were refit. An array of 7×7 towers were summed. The absence of the steel plate results in decreased values for both offset ($\delta = 0.10 \pm 0.03$ GeV) and the resolution sampling term ($S = 0.133 \pm 0.013$). At $\eta = 2.55$, electrons traverse an additional 0.4 X_0 of aluminum, and this additional material results in increased values of the offset ($\delta = 0.43 \pm 0.02$ GeV) and the resolution sampling term ($S = 0.166 \pm 0.003$). An array of 11×11 was used in analysis of the energy scan data at this last value of η where the towers attain their smallest transverse size. The linearity of the response of the calorimeter at these two values of η was similar to that found at the benchmark (Fig. 20a).

3.6 Position Resolution

The centroid of an electromagnetic shower can be determined to much better accuracy than one would naively calculate based on the calorimeter segmentation, due to the transverse spread of the shower which results in sharing of the energy among several towers. In the ECEM most of the energy is deposited in EM3, which has a transverse segmentation of 0.05 in both η and ϕ; this finer segmentation improves the position measurement. The transverse projection of an electromagnetic shower

in EM3 can be characterized by the sum of two exponentials:

$$\frac{dE}{dx} = A_1 \exp\frac{-|x-x_0|}{B_1} + A_2 \exp\frac{-|x-x_0|}{B_2}, \tag{7}$$

where x represents either the radial or azimuthal coordinate, and x_0 is the impact position of the shower. In this expression the first term corresponds to the shower core while the second term corresponds to the shower tails. For a 50 GeV shower at $\eta = 1.95$, a fit to Eq. 7 yields $A_1/A_2 = 3.7 \pm 0.1$, $B_1 = 2.9 \pm 0.1$ mm and $B_2 = 11.1 \pm 0.1$ mm. The parameters of the fit vary with both the energy and incident angle of the shower.

The transverse electromagnetic shower profile in EM3 is shown in Fig. 21. The fraction of the total energy deposited in EM3 in all towers a distance $\geq x$ away from the impact position of the shower is plotted as a function of $x = r \cdot \phi$. In this plot, the tower structure of the ECEM has been used to integrate the energy along towers using the straight lines which separate towers in azimuth(ϕ). For this analysis, where we are dealing with the signal in the tail of the shower, we increased the threshold suppression level to remove channels within $\pm 3\sigma$ of their pedestal value, in order to better compare the experimental data with the Monte Carlo simulation which did not include electronic or uranium radioactivity-induced noise. Although the agreement between data and Monte Carlo is reasonably good, the transverse shape in the data appears to be slightly broader than in the Monte Carlo.

Several techniques are available for extracting the point of impact of an electromagnetic shower [17]; we have investigated two algorithms which give satisfactory results. In the first method, the tower containing the maximum energy in EM3 is identified and all the energy to the right of this tower (in either η or ϕ) is summed up and denoted E_R. The ratio of E_R to E_T, where E_T is the sum of all energy deposited in EM3, is then given by:

$$\frac{E_R}{E_T} = \frac{\int_0^\infty \frac{dE}{dx}dx}{\int_{-\infty}^\infty \frac{dE}{dx}dx} = \frac{A_1B_1 \exp\frac{-|x_0|}{B_1} + A_2B_2 \exp\frac{-|x_0|}{B_2}}{2(A_1B_1 + A_2B_2)}. \tag{8}$$

Eq. 8 holds for $x_0 < 0$, where $x = 0$ is defined to be the edge of the tower. (For $x_0 > 0$, subtract Eq. 8 from 1.) Given the parameters A_1, A_2, B_1 and B_2, determined from fits to the transverse shape of the shower, one can extract $|x_0|$ from the ratio of E_R/E_T by iterative approximation.

In the second method, a first estimate of the position is made by calculating the energy weighted center-of-gravity of the shower,

$$x_{cog} = \frac{\sum x_i E_i}{\sum E_i}, \tag{9}$$

where x_i is the position of the center of the tower containing energy E_i in η or ϕ. This first estimate, which suffers from large systematic deviations from the true position, is then corrected to x_{ccog} using the following algorithm:

$$x_{ccog} = x_m + B \cdot \sinh^{-1}\{\frac{(x_{cog} - x_m)}{\Delta} \cdot \sinh(\frac{\Delta}{B})\}. \quad (10)$$

In this expression, x_m is the position of the center of the EM3 tower that has the largest signal, Δ is the tower half-width, and B characterizes the transverse shower shape assuming a single exponential fall-off. In principle, B can be calculated as the weighted sum of two exponentials, but in practice B was used as a free parameter which was optimized to obtain the best position resolution. A value of $B = 5$ mm was found to give good results for energies ranging from 10 GeV to 150 GeV, and for all values of η. In the azimuthal direction, a further improvement in position resolution was obtained by letting B be a linear function of the distance from the pad edge, d, reaching a minimum of 3.5 mm at $d = 0$ and increasing to a maximum value of 5 mm at $d = 2$ cm. In the radial direction, the best results were obtained using a constant value of $B = 5$ mm, but correcting the radial coordinate, r, as: $r_{\text{corrected}} = r - 0.15\,|d|$.

To determine the position resolution of the ECEM, electron trajectories were extrapolated to the middle of EM3 using PWCs located upstream in the beamline. The extrapolated position was known to a precision of approximately 400 μm, which is significantly better than the position resolution of the ECEM; however the overall offset between the PWCs and the ECEM had an uncertainty of several mm, so the absolute position was determined using the ECEM itself. A Gaussian fit to the difference between the measured impact positions in EM3 and their extrapolated values was used to determine the position resolution of the calorimeter (Fig. 22). The two different techniques for position determination described above yielded very similar results; for simplicity in what follows we will show only the results for the corrected center-of-gravity.

The best position resolution is obtained when the shower is centered between two towers; this is shown in Fig. 23 where the position resolution is given as a function of distance from the edge of a tower, for 50 GeV e^-. The fit shown is to a function of the form $\sigma(\text{in mm}) = 1.0 + 0.0035x^2$, where x is the distance (in mm) from the edge of a tower. Due to the variation in resolution with distance from the edge of a tower, one expects to see the position resolution improve as the tower size decreases. However, the effect in the ECEM is not very pronounced; based on the quadratic

dependence given above, we would expect the resolution to improve by less than 0.2 mm over the η range from 1.8 to 3.2. Our measured resolutions are consistent with this, within errors.

The measured position resolution is also a function of energy; in fact, due to the inherently statistical nature of shower development, we expect a resolution which varies as $E^{-0.5}$. In Fig. 24 we show the energy dependence of the azimuthal position resolution at η=1.95, for the corrected center-of-gravity technique. (The azimuthal position resolution is given in mm, by taking the product of the radius, in mm, with the azimuth, in radians.) Both the resolution at the edge of a tower and the resolution averaged over several towers are shown. (The towers in EM3 at η=1.95 are approximately 25 $\times$ 25 mm^2.) The energy dependence of the position resolution of the radial coordinate is similar to that of the azimuthal coordinate.

3.7 Uniformity of Response

Because the ECEM module is constructed as a single unit, the calorimeter response is expected to be uniform over almost all of its area. The only two structural features that affect the response are: a) the small gap between the central and side uranium plates, and b) the tie-rods. In this section, we present results of uniformity studies away from these singular regions, using scans with 100 GeV electrons in the η and ϕ directions. Data taken with beam directed at the gap in the uranium plates and at the tie rods will be discussed in the next section.

Because the construction of the ECEM is symmetric in azimuth, the response of the ECEM is expected to be uniform in this coordinate (ϕ). The mean pulse height as a function of azimuth is shown in Figs. 25a and 25b for $\eta = 1.85$ and 1.95, respectively. The azimuth is given as the arc length of the calorimeter s (mm) = R (mm)$\times\phi$ (rad), where at $\eta = 1.95$, the radius, R, is approximately 520 mm. For both scans, the mean response is constant to 0.4% (rms).

The situation is slightly more complicated when scanning in η: in addition to changing the impact point on the module, the amount of material upstream of the calorimeter changes, and the number of towers needed for lateral containment also changes because the pads become smaller as η increases. Rather than using the $n \times n$ tower arrays discussed above, in this analysis the entire instrumented section of the calorimeter was summed for each event.

The results from a scan in the η direction is shown in Fig. 26a. (The missing points at $\eta \sim 2.4$ correspond to the gap between the uranium plates.) The results

shown in Fig. 26a were obtained using a single set of calibration constants (the α, β, and δ obtained at the $\eta = 1.95$ benchmark) for all values of η. A more uniform response is achieved (Fig. 26b) by using the slopes and offsets listed in Table 5 (but always the same set of layer weights (β_j)), for values of η with different amounts of material upstream of the ECEM module. The high point at η=1.65 and the fall-off in response for $\eta < 1.60$ are due to module edge effects. (Note that this is an artifact of the test beam configuration. At D0, shower leakage out of the ECEM module is measured in the Middle Hadronic modules.) For $\eta > 1.65$ the response is found to be uniform to 0.4% (rms).

3.8 Scans Across the Uranium Gap and Across the Tie-rods

As described in Sec. 2.3, the construction of the uranium absorber disks (Fig. 6) results in small (nominal width 1 mm) gaps at $x = \pm 33.5$ cm, where x is the horizontal coordinate measured from the beam axis. These gaps are not projective, that is, all the central plates have the same width, and all the disks have the same orientation (with the gaps vertical).

Fig. 27 shows the calorimeter response for 100 GeV electron beams plotted as a function of the x coordinate of the shower in the vicinity of the gap in the uranium plates. The increase in the signal has a maximum of 5% and a full width at half maximum (FWHM) of 1.4 cm. The effect of both gaps (i.e. at $\pm x$) is small: 2.5% of the active area of the ECEM module has an increase in signal $\geq 1\%$. The correction to the energy of electromagnetic showers in the vicinity of these gaps is straightforward and is very well modeled by the Monte Carlo simulation, as shown by the histogram in Fig. 27. This increase in signal is thought to have two causes: a) because of the long (2.2 μs) integration time, the amplifiers can collect the additional ionization produced within the gap between the plates, and b) the sampling fraction of the calorimeter is increased locally because of the absence of uranium in the crack.

The tie-rods, which were described in Sec. 2.4, are another source of non-uniformity in the calorimeter response. These titanium bolts are parallel to the beam (z) axis, and therefore are not projective from the interaction point. In order to study the effect of the tie-rod assemblies on the calorimeter response, we took data with 100 GeV electrons scanning in both the azimuthal and radial directions across a tie-rod located at η=2.05. Data was taken with the beam incident on the tie-rod at different angles, corresponding to interaction vertices at the Tevatron collider of $z = 0, \pm 30$ cm. The

results presented here were obtained with an interaction vertex of $z = +30$ cm, as shown in Fig. 28.

The results from the azimuthal scan are shown in Fig. 29a. The radial scan results are shown in Fig. 29b, where the mean pulse height is shown as a function of the polar angle (θ) from the beam axis. The dotted lines indicate the angle where the projected track crosses the boundary of the 20 mm diameter circular area where the high voltage bearing resistive coat has been removed from the signal disks. Also shown are the results from a Monte Carlo simulation that included a simplified model of the components shown in the detail of Fig. 9. The decrease in the signal in the vicinity of the tie-rod, 15% at maximum, is reproduced very well by the Monte Carlo. From this measurement of the response function we estimate that the effect of the 96 tie-rods is that 8% (1.5%) of the active area of the ECEM has a loss of signal greater than 1% (5%).

The shape (Fig. 29b) of the response as a function of the polar angle results from summing the four longitudinal sections. The response functions for the individual sections are shown in Fig. 30a–d, where the dotted lines again indicate the boundary of the 20 mm diameter zone with the resistive coat removed. Where the core of the shower is incident on the bolt, the signals in the first three sections decrease, while the signal in the last section increases because the low Z material of the tie-rod assembly results in delayed shower development. The Monte Carlo simulation again reproduces very well the response functions of the individual sections.

3.9 e/π Discrimination

The electron-pion (e/π) discrimination for isolated particles was studied by comparing electron and pion data at seven momenta ranging from 10 to 150 GeV/c at $\eta = 1.95$. We separate electrons from pions based on the ratio of hadronic (HAD) to electromagnetic (EM) energy, and on the basis of the covariance matrix method suggested by Engelmann *et al.*[18]. The EM energy is calculated by summing the ADC counts from all four longitudinal sections of ECEM in a 5×5 array of 0.1×0.1 towers, centered on the tower containing the largest signal. (This array size was found to give the best e/π discrimination at $\eta = 1.95$.) The HAD energy was calculated by summing the ADC counts from all five longitudinal sections of the ECIH for the same towers used to reconstruct the EM energy. The ECIH layers were weighted relative to the ECEM by the relative inverse sampling fractions which were calculated using the minimum ionizing dE/dX values. Figs. 31a and 31b show the distributions of

HAD/EM for 100 GeV/c electrons and pions. A cut of HAD/EM<0.02 provides a π rejection factor of 300 and an electron efficiency of 95%.

We were able to improve on the simple HAD/EM cut by following it with an application of the covariance-matrix method, which takes full advantage of the fine longitudinal and transverse segmentation of the ECEM. Using "training samples" of electrons, we constructed a 72×72 covariance matrix V for all channels (or pads) in the four ECEM longitudinal sections plus the first ECIH section (the EM3 section has four readout channels because of its finer transverse segmentation) within a 3×3 array of towers centered on the tower containing the maximum energy:

$$\mathrm{V}_{ij}(p) = \frac{1}{\mathrm{N}} \sum_{n=1}^{\mathrm{N}} (Q_i^{(n)} - < Q_i >)(Q_j^{(n)} - < Q_j >) \; ; \; (i,j = 1,...,72), \qquad (11)$$

where p is the electron momentum, the Q_i correspond to the ADC counts in the i-th channel for the n-th electron event (total number of events is N) and $< Q_i >$ is the mean value of Q_i over N events. This matrix contains information on both longitudinal and transverse profiles of electromagnetic showers including correlations between different longitudinal and transverse sections. The inverse matrix $\mathrm{H} = \mathrm{V}^{-1}$ was used to compute a test variable ζ for a given event k;

$$\zeta = \sum_{i,j} (Q_i^{(k)} - < Q_i >)\mathrm{H}_{ij}(p)(Q_j^{(k)} - < Q_j >) \; ; \; (i,j = 1,...,72). \qquad (12)$$

The matrix elements are momentum dependent, and we determined seven sets of elements from electron data at seven momenta. The elements corresponding to intermediate momenta were obtained by linear interpolation. Proceeding in a manner applicable to DØ, where the particle momentum is not measured (except for muons), we used the *observed* EM energy to interpolate the matrix elements when calculating ζ.

Using an independent sample of electrons, the HAD/EM and ζ criteria were determined to obtain a given overall electron efficiency. A combination of HAD/EM< 0.04 and $\zeta < 200 - 320$ (depending on the EM energy) was found to provide an electron efficiency of 95%. The distribution of ζ for 100 GeV electrons is shown in Fig. 32. The resulting rejection factor is shown in Fig. 33 together with the result obtained by the HAD/EM cut alone. The π rejection factor is given for 95% electron efficiency. The rejection factor plotted at a given momentum is the inverse of the probability that a pion of this momentum will be reconstructed as an electron of *any* energy. This follows from the fact that HAD/EM and ζ were calculated using *only* the energy

observed in the calorimeter. The results at higher momenta ($\geq$ 100 GeV/c) are given as lower limits at a 90% confidence level due to the limited statistics of the pion data sample ($\sim$ 3200 – 6500 events/momentum). The covariance matrix method significantly improves the pion rejection over the HAD/EM cut. The π rejection factor is approximately 900 – 3000 for particles in the momentum range between 50 to 150 GeV/c.

4 Summary

The electromagnetic modules for the two DØ End Calorimeters have been constructed and installed in the DØ cryostats in preparation for the experiment's first run at the Fermilab Tevatron Collider. These modules were constructed as monolithic units by assembling the uranium absorber plates and multilayer signal boards into disks. A beam test was performed with a completed ECEM module and the main results obtained with electron beams are:

- The response is linear to $\leq \pm 0.3\%$ for electron energies $10 \leq E \leq 150$ GeV.
- The energy resolution sampling term is $(0.157 \pm 0.006)/\sqrt{E}$ (where E is in GeV), and the constant term is consistent with zero (0.003 ± 0.003).
- The average position resolution obtained using a corrected center of gravity algorithm is 0.8 mm for 100 GeV electrons and has an energy dependence given by $\sigma(\text{mm}) = 16.6/E^{0.66}$, where E is in GeV.
- Scanning both azimuthally and radially, the response is uniform to $\leq$ 0.4% (rms) for $\eta > 1.6$.
- From the combined response of the ECEM and the hadronic module behind it, a pion rejection factor of $\sim 900 - 3000$ is obtained for particles with momentum $>$ 50 GeV/c (at 95% electron efficiency) using a covariance matrix technique.
- Agreement with Monte Carlo simulations is found for transverse and longitudinal shower profiles, energy resolution, and for the module response near its structural features.

This work was supported by the U.S. Department of Energy and the National Science Foundation. We would like to thank A. Allen, K. Ganga, L. Goddard, M. Hoff, J. Hunter, Y. Minamihara, R. Smits, D. Worth, J. Yamada, and the LBL

Assembly Shop for their help in the design, construction, and testing of this detector. We are also grateful for the support from the Accelerator and Research Divisions at Fermilab.

References

[1] Design Report for the DØ Experiment at the Fermilab Antiproton-Proton Collider, Fermilab, November 1984 (unpublished).

[2] P.D. Grannis, in "Proceedings of Les Rencontres de Physique de la Vallée d'Aoste on Results and Perspectives in Particle Physics", La Thuile, March 1987, edited by M. Greco (Editions Frontières, 1987) p. 253.

[3] S. Abachi *et al.,* FNAL-PUB-92/162, submitted to Nucl. Instr. and Meth.

[4] General Circuits, Inc., Menlo Park, Ca., USA., and Buckee-Mears St. Paul, St. Paul, Minn., USA.

[5] Abatron Inc., Gilberts, Il., USA. See C. Escobar, *et al.*, DØ Note 285 (1985) (unpublished) for details.

[6] Manufacturing Sciences Corporation, Oak Ridge, Tenn., USA.

[7] A.G. Ritchie, J. Nucl. Mater. **102** (1981) 170.

[8] Lenthor, Milpitas, Ca., USA.

[9] A possible explanation for this phenomenon is considered in R. McCarthy, DØ Note 780 (1988) (unpublished), and M.L. Stevenson, DØ Note 1154 (1991) (unpublished).

[10] M. Demarteau, in "Proceedings of the First International Conference on Calorimetry in High Energy Physics", Fermilab, Oct. 1990, edited by D. Anderson *et al.,* (World Scientific, 1991) p. 91.

[11] P. Franzini, Nucl. Instr. and Meth. **A289** (1990) 438.

[12] D. Huffman, FERMILAB-CONF-91-344, Dec 1991, Presented at IEEE Nuclear Science Symp., Santa Fe, N.M., Nov 5-9, 1991.

[13] R. Brun *et al.,* CERN-DD/EE/84-1, May 1986.

[14] J. Engler *et al.,* Nucl. Instr. and Meth. **120** (1974) 157.

[15] G. Blazey, in "Proceedings of the First International Conference on Calorimetry in High Energy Physics", Fermilab, Oct. 1990, edited by D. Anderson *et al.,* (World Scientific, 1991) p. 101.

[16] J.E. Moyal, Phil. Mag. **46** (1955) 263.

[17] G.A. Akopdjanov *et al.,* Nucl. Instr. and Meth. **140** (1977) 441; A. DeAngelis and F. Mazzone, Nucl. Instr. and Meth. **A287** (1990) 397.

[18] R. Engelmann *et al.,* Nucl. Instr. and Meth. **216** (1983) 45.

Table 1: ECEM Module Parameters

	Longitudinal Depth Segment				TOTAL
	EM1	EM2	EM3	EM4	
Number of cells	2	2	6	8	18
Transverse Segmentation: $(\Delta\eta \times \Delta\phi)$	$0.1 \times \pi/32$	$0.1 \times \pi/32$	$0.05 \times \pi/64$	$0.1 \times \pi/32$	
Number of readout channels	1248	1248	3680	1312	7488
Dimensions:					
Inner Radius [cm]	5.7	5.7	5.7	5.7	
Outer Radius [cm]	83.2	89.3	97.5	103.9	
Mean position along beam-line [cm]	171.6	174.0	179.1	189.3	
Absorber: material	Fe	U	U	U	
thickness [mm]	1.4	4.0	4.0	4.0	
Radiation Lengths [X_0]	0.3	2.6	7.9	9.3	20.1
Interaction Lengths [λ_{int}]	0.05	0.10	0.31	0.48	0.94
Capacitance Range (nF) (Module only)	0.2-0.9	0.3-1.0	0.7-1.5	1.2-4.8	

Table 2: Longitudinal Profile for 50 GeV electrons: The fraction of the total signal in each layer.

Layer	Data	Monte Carlo
EM1	0.0436 ± 0.0003	0.0449 ± 0.0008
EM2	0.1775 ± 0.0008	0.1718 ± 0.0022
EM3	0.6482 ± 0.0009	0.6472 ± 0.0022
EM4	0.1273 ± 0.0009	0.1326 ± 0.0026
IH1	0.0036 ± 0.0003	0.0035 ± 0.0014

Table 3: The sampling fractions (SF) calculated for a minimum ionizing particle, these values normalized to the third EM layer ($SF(3)/SF(j)$), and the layer weights (β_j) found from the resolution/linearity minimization. The dE/dX values for the first readout layer (EM1) include the material upstream of the module. The values in parentheses were not varied in the fit.

	dE/dX		Data	Monte Carlo
Layer	SF	$\frac{SF(3)}{SF(j)}$	β_j	β_j
EM1	.049	1.83	1.47±.03	1.13±.03
EM2	.088	1.01	1.00±.01	0.98±.01
EM3	.089	1.00	(1.0)	(1.0)
EM4	.081	1.10	1.10±.01	1.04±.01
IH1	.053	1.67	(1.67)	(1.67)

Table 4: Energy resolution fit results.

	Data	Monte Carlo
C	0.003±0.003	0.000±0.016
$S(\sqrt{GeV})$	0.157±0.006	0.153±0.002
$N(GeV)$	0.29±0.03	–

Table 5: Energy scan slopes and offsets.

η	Upstream Material X_0	$\alpha \times 10^3$ (GeV/ADC)	δ GeV
1.95	2.31	3.742±.008	0.30±.02
2.10	0.70	3.788±.002	0.10±.03
2.55	2.71	3.760±.002	0.43±.02

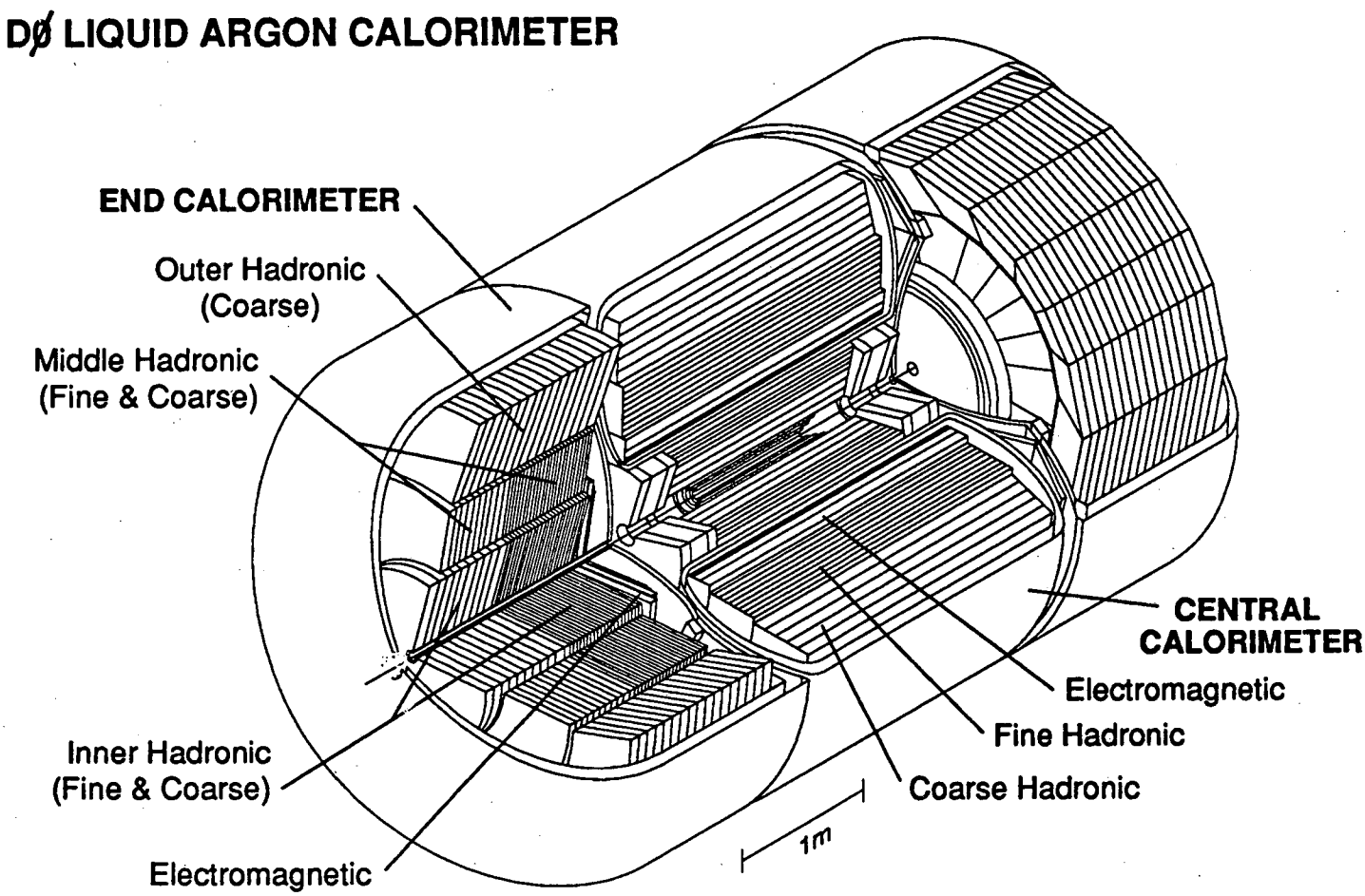

Figure 1: The various modules that comprise the DØ Central and End Calorimeters.

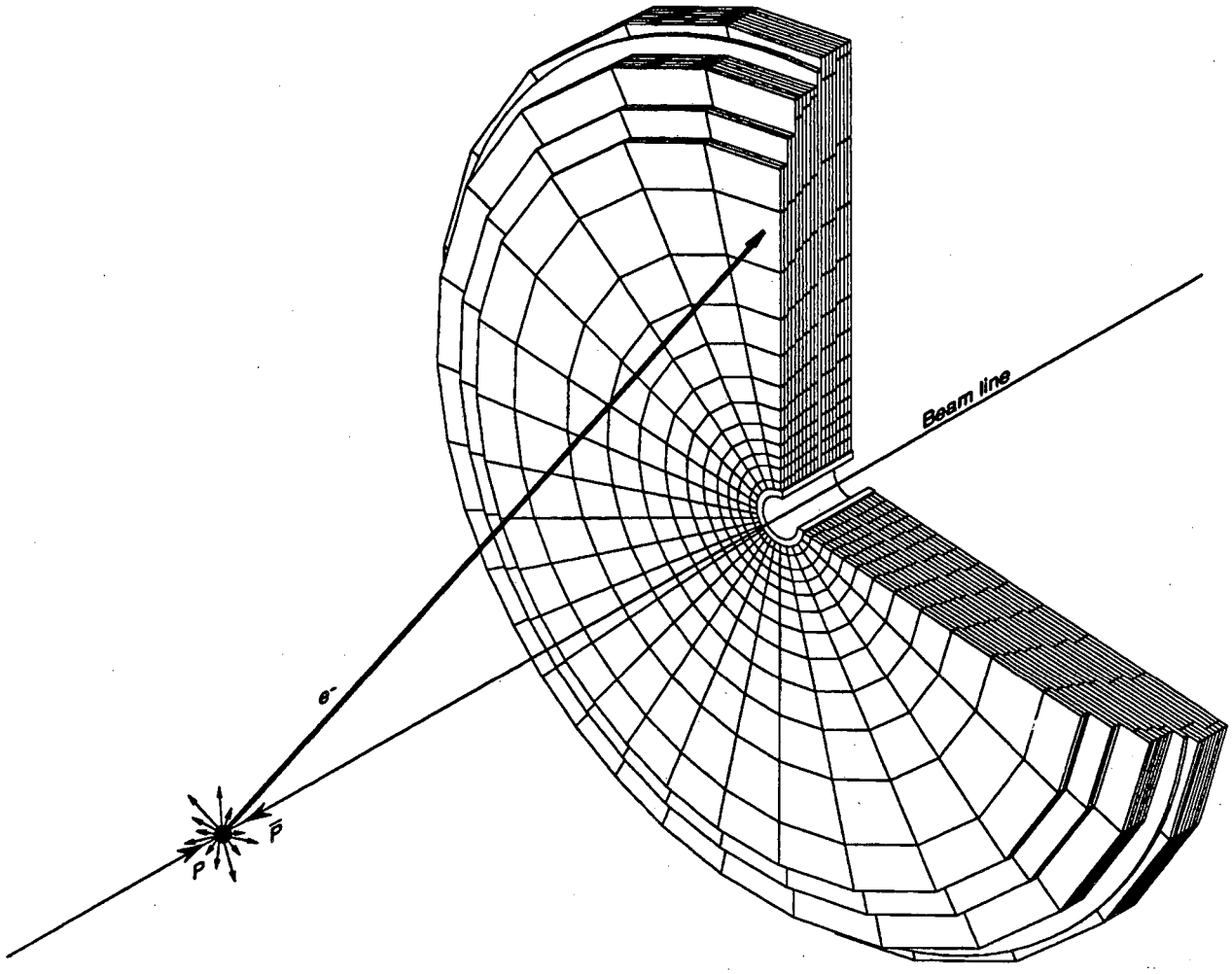

Figure 2: Cut-away view of the ECEM module.

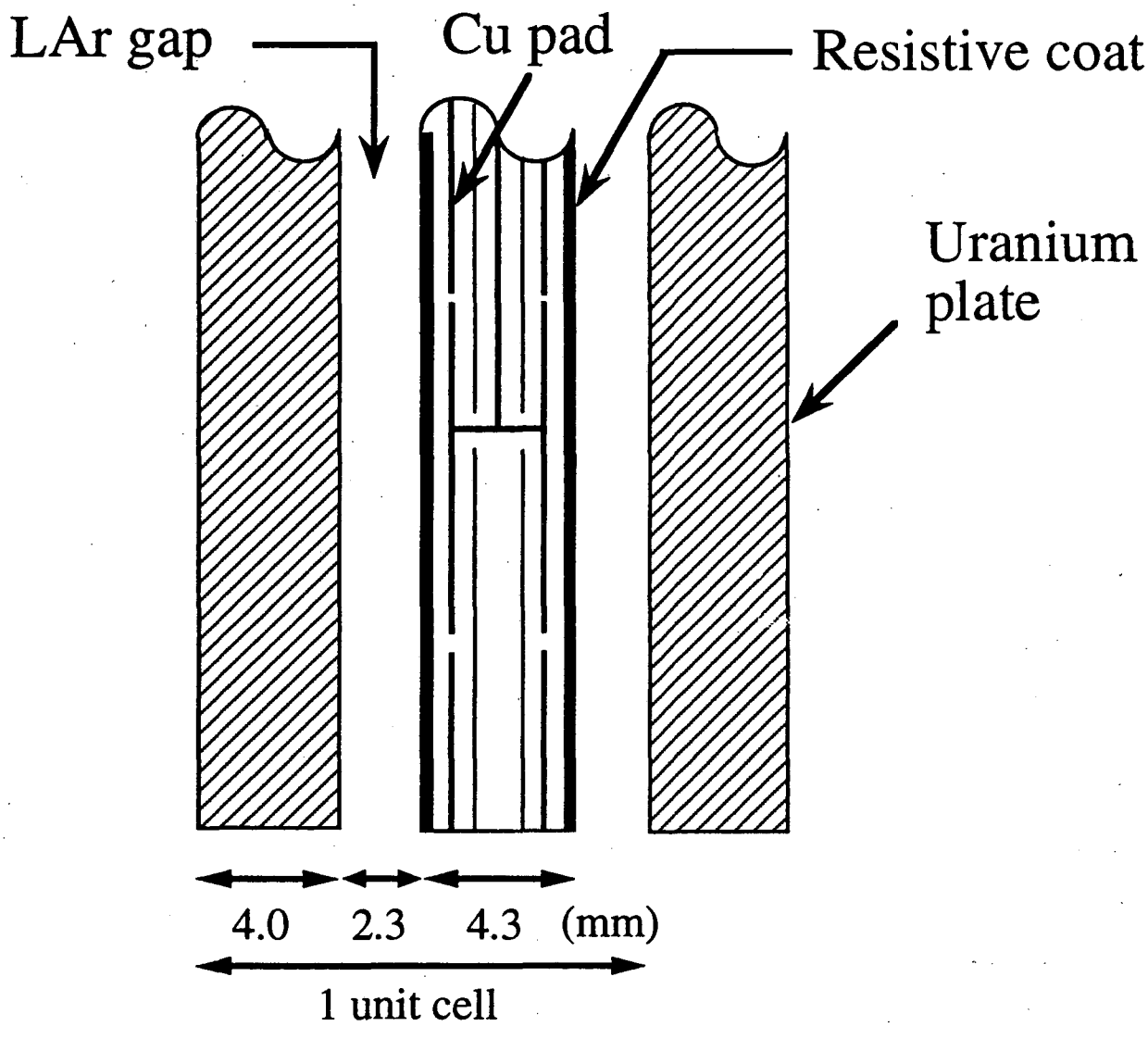

Figure 3: The composition of the basic sampling cell of the ECEM module.

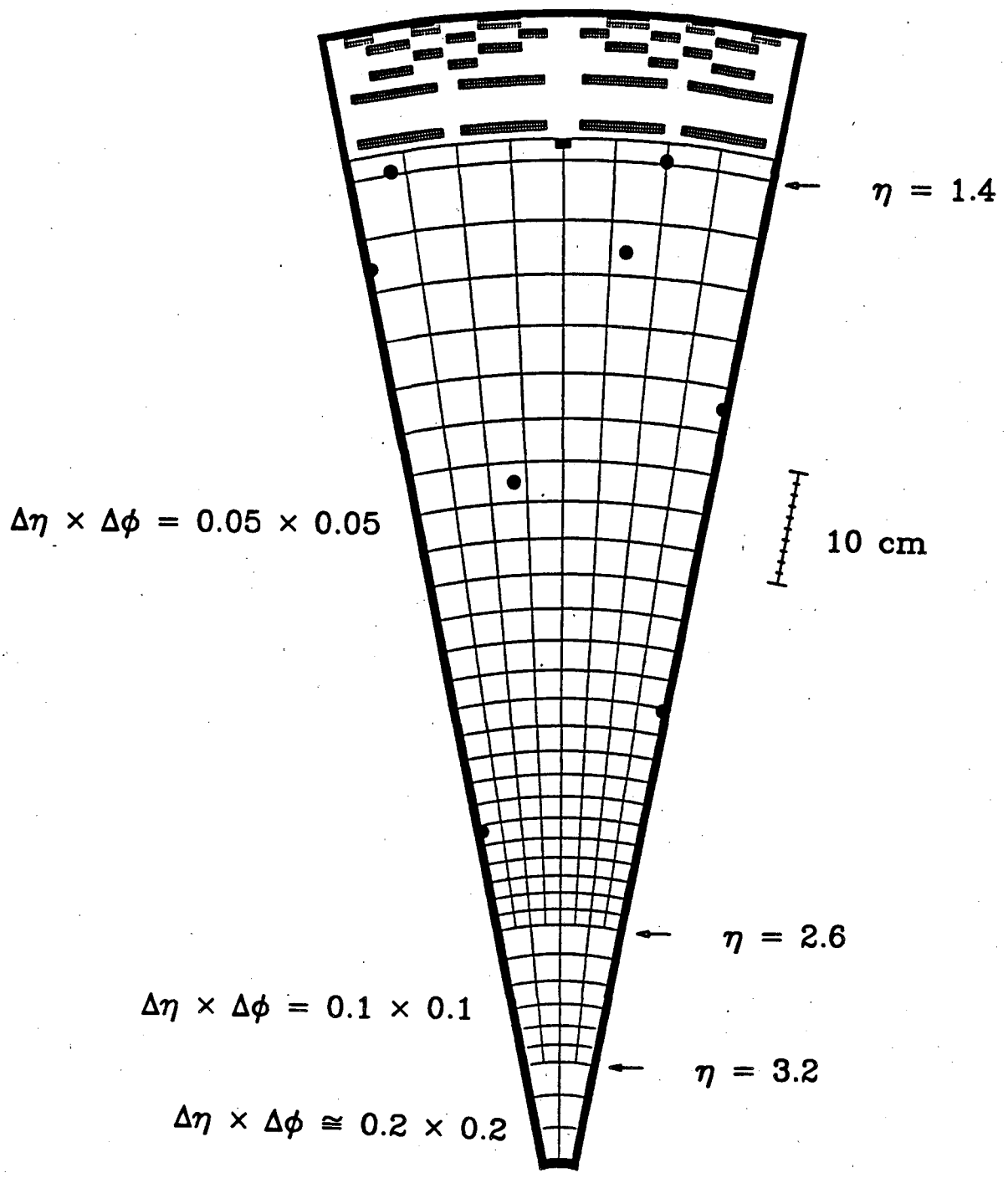

Figure 4: The pad layout of a 22.5° multilayer signal board of the third longitudinal section (EM3) of the ECEM module. The small dark circles are where the signal pad has been removed for the tie-rods.

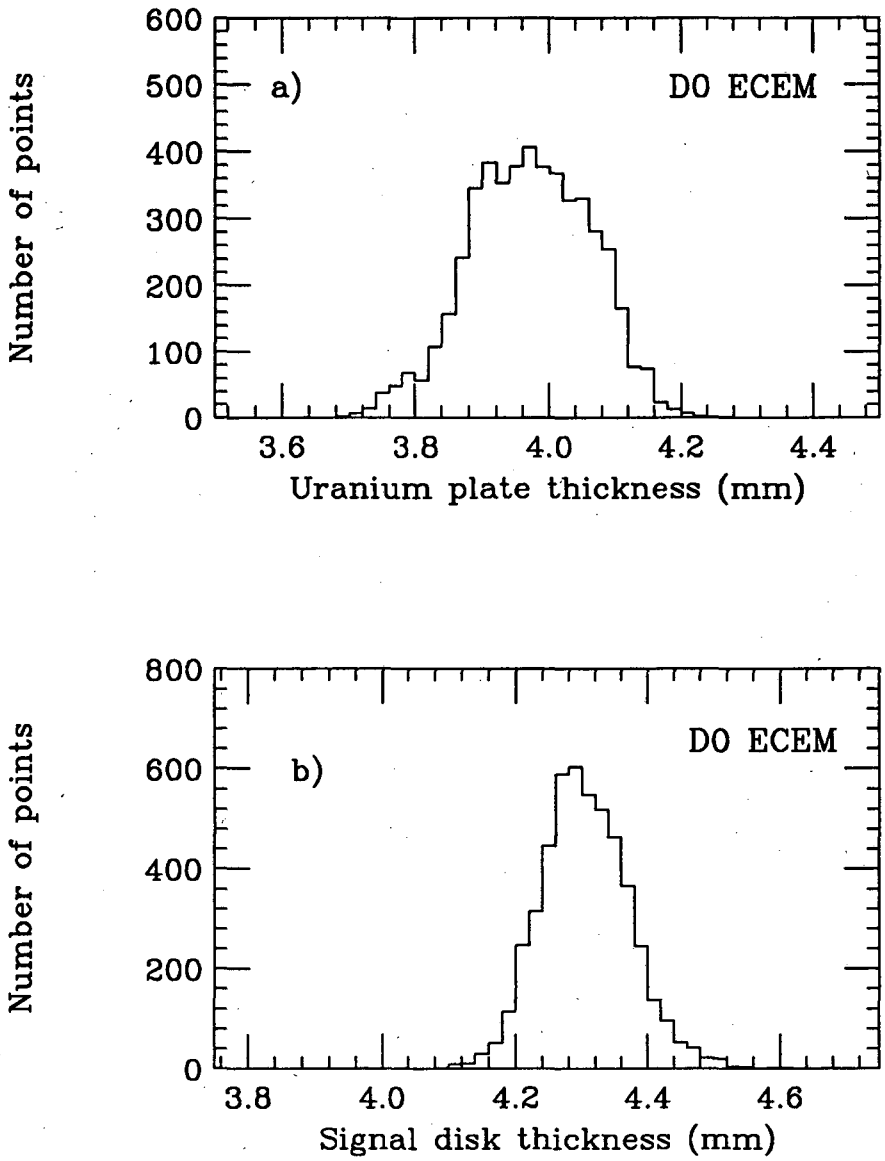

Figure 7: The measured thickness distributions of the a) uranium plates (mean 3.97 mm, rms 0.09 mm) and b) signal disks (mean 4.31, rms 0.06 mm).

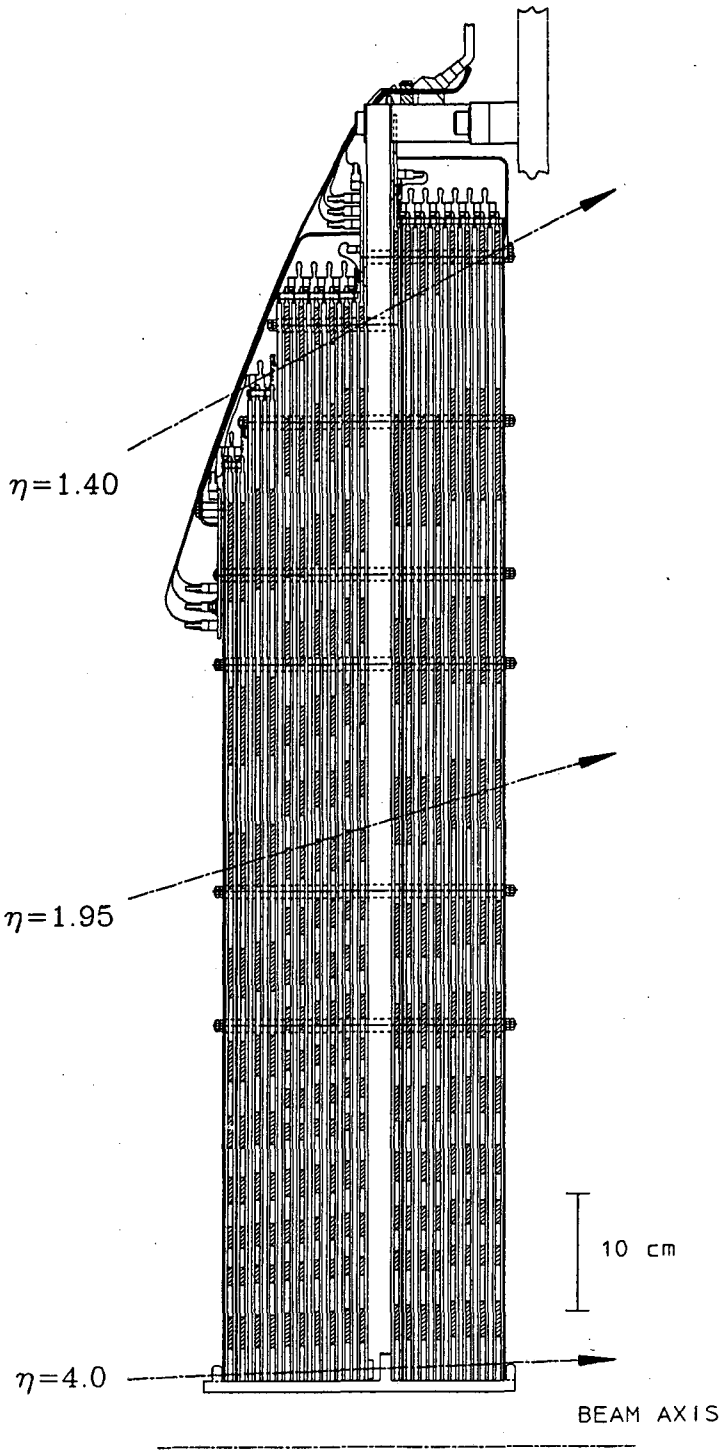

Figure 8: Cross sectional view of the upper half of the ECEM module.

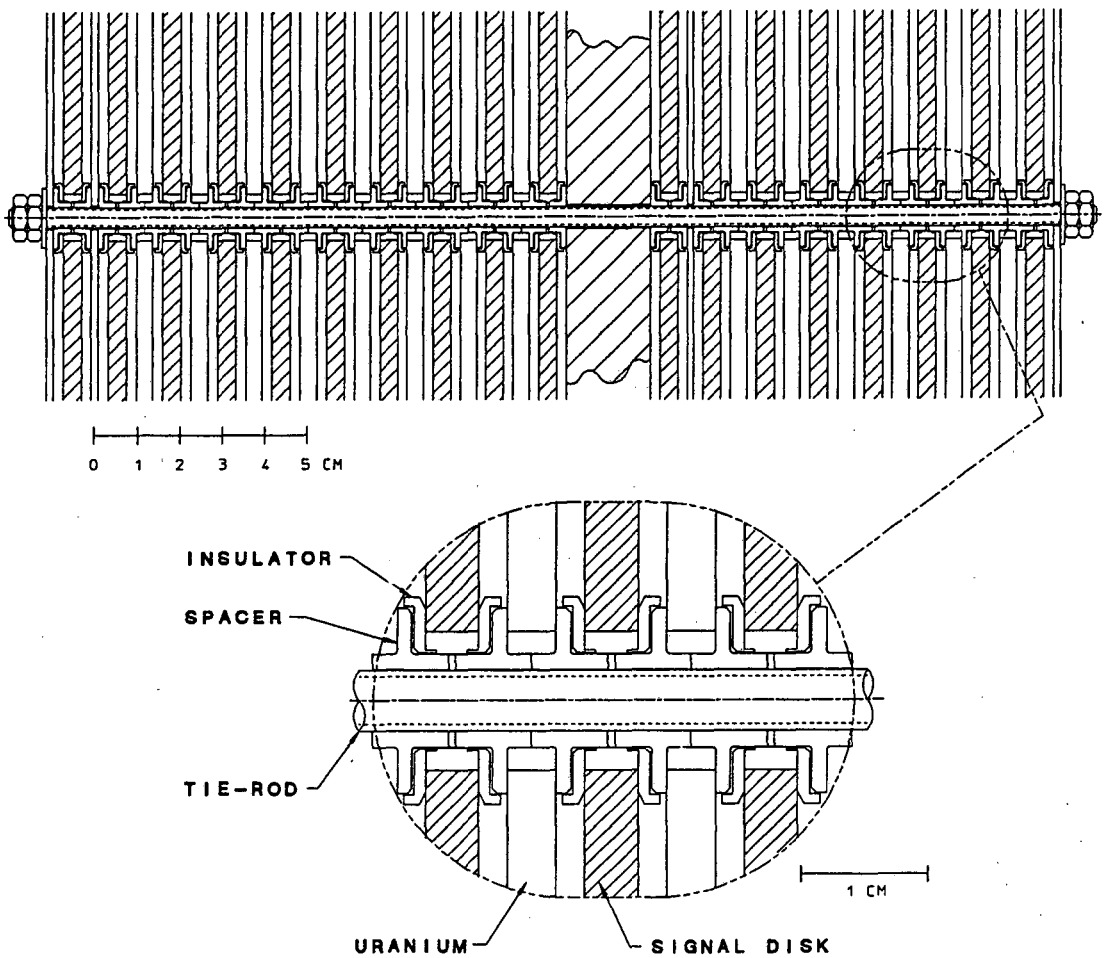

Figure 9: Cross sectional view of a tie-rod assembly.

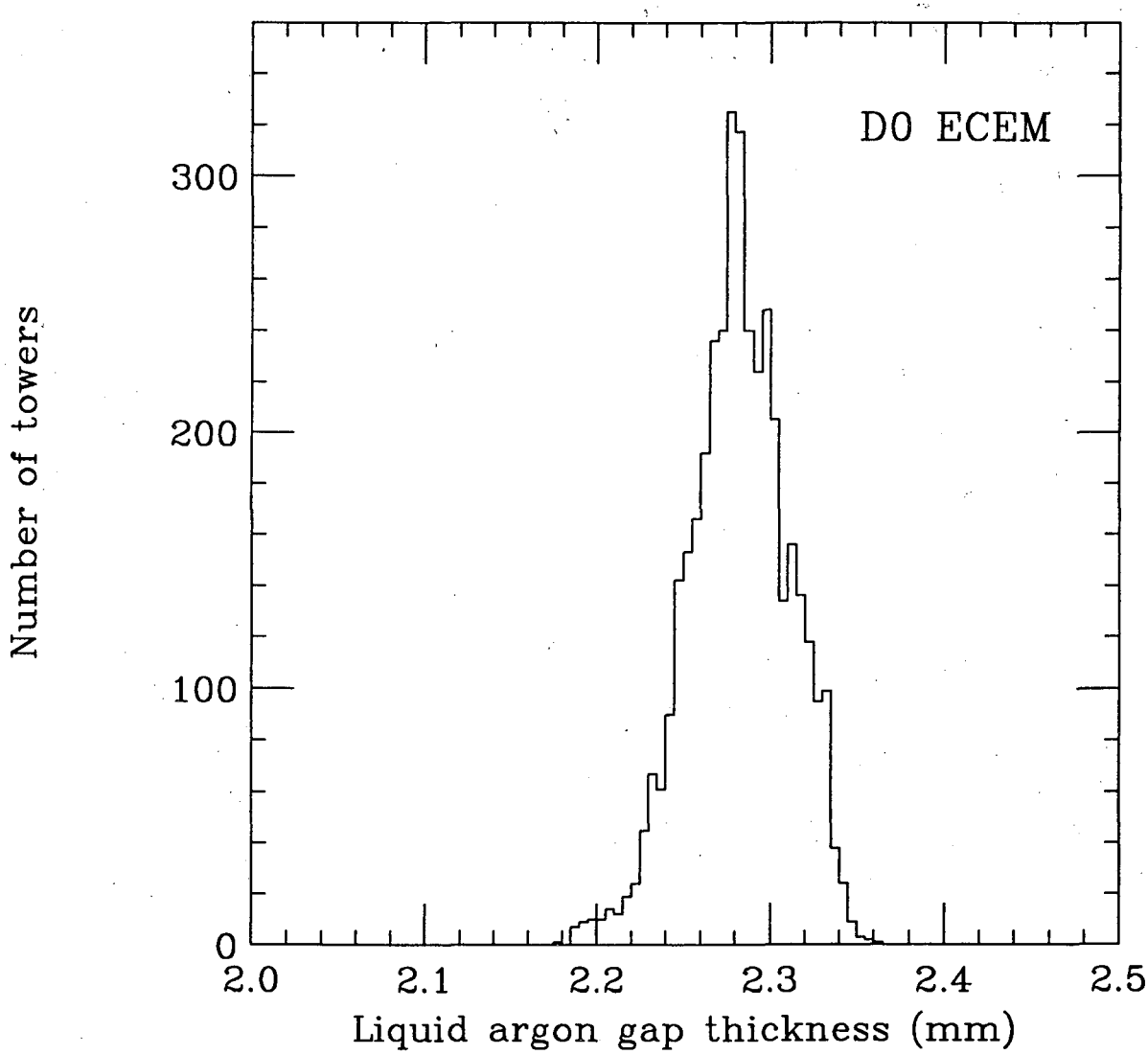

Figure 10: The calculated mean thickness of the liquid argon gaps for all towers. The mean is 2.28 mm and the rms is 0.03 mm.

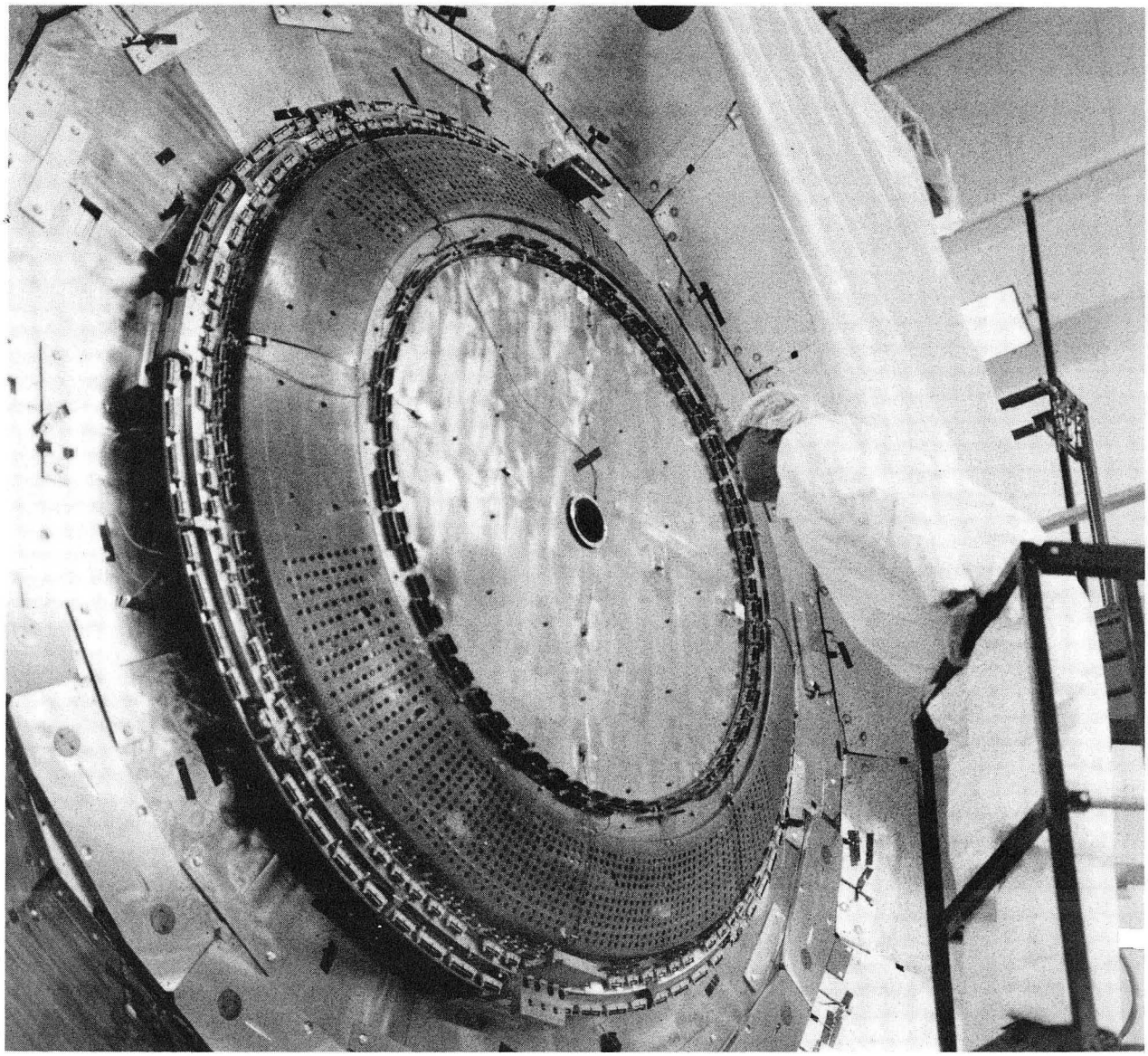

Figure 11: The ECEM module mounted onto the hadronic modules in the DØ End Calorimeter prior to final cabling.

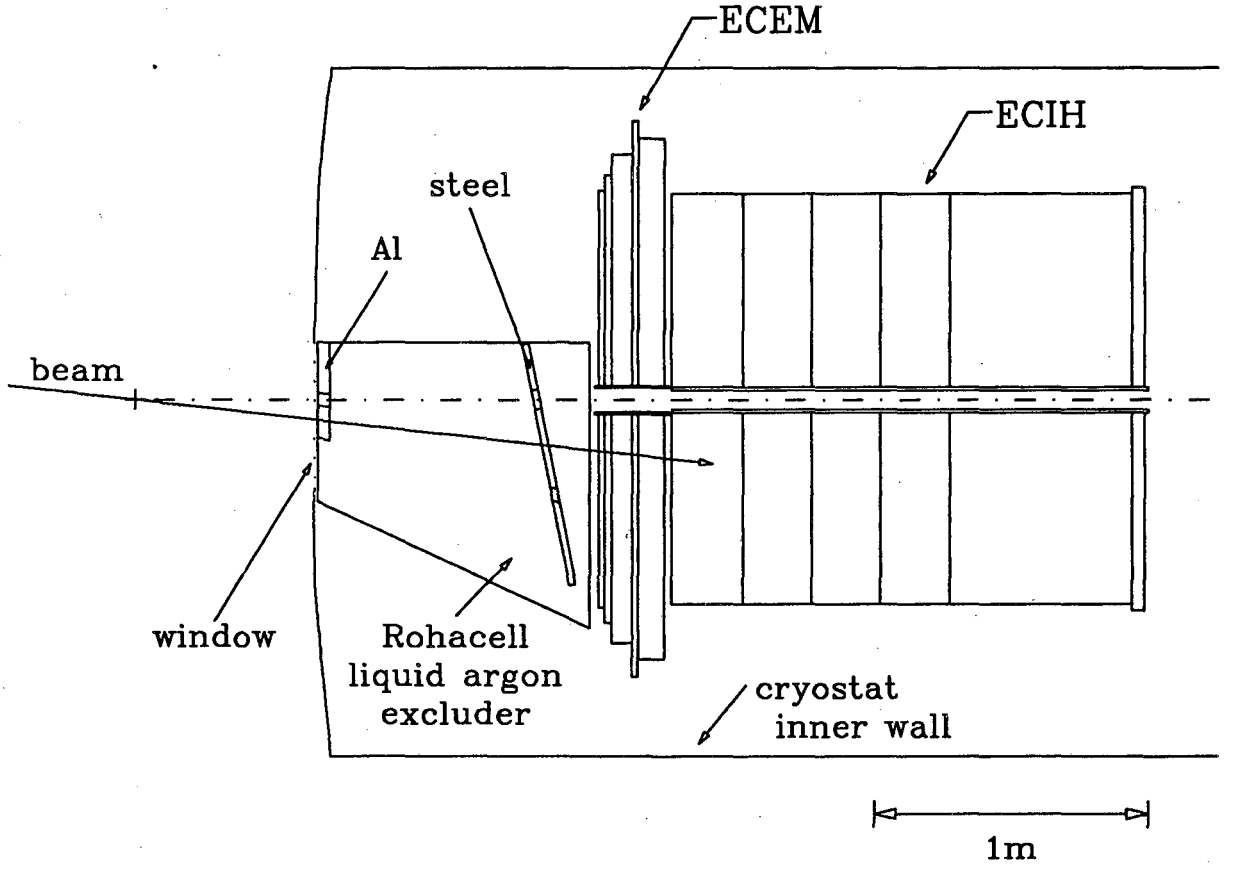

Figure 12: Plan view of the configuration of the calorimeter modules in the test beam.

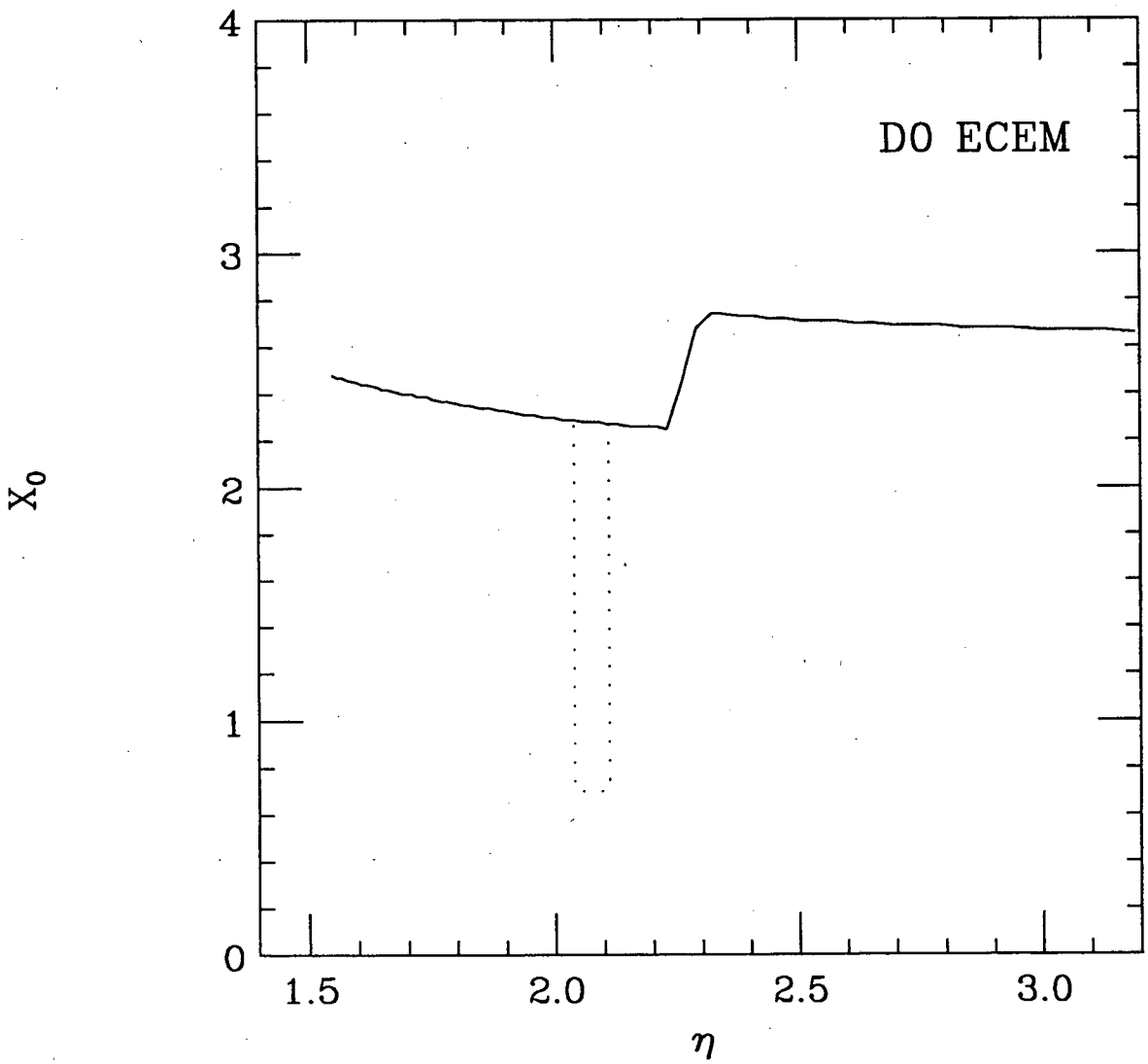

Figure 13: Estimate of the amount of material in radiation lengths (X_0) upstream of the front face of the ECEM module in the test beam cryostat. The dotted lines indicate the location of the 5 cm diameter hole in the steel plate discussed in Sec. 3.5.

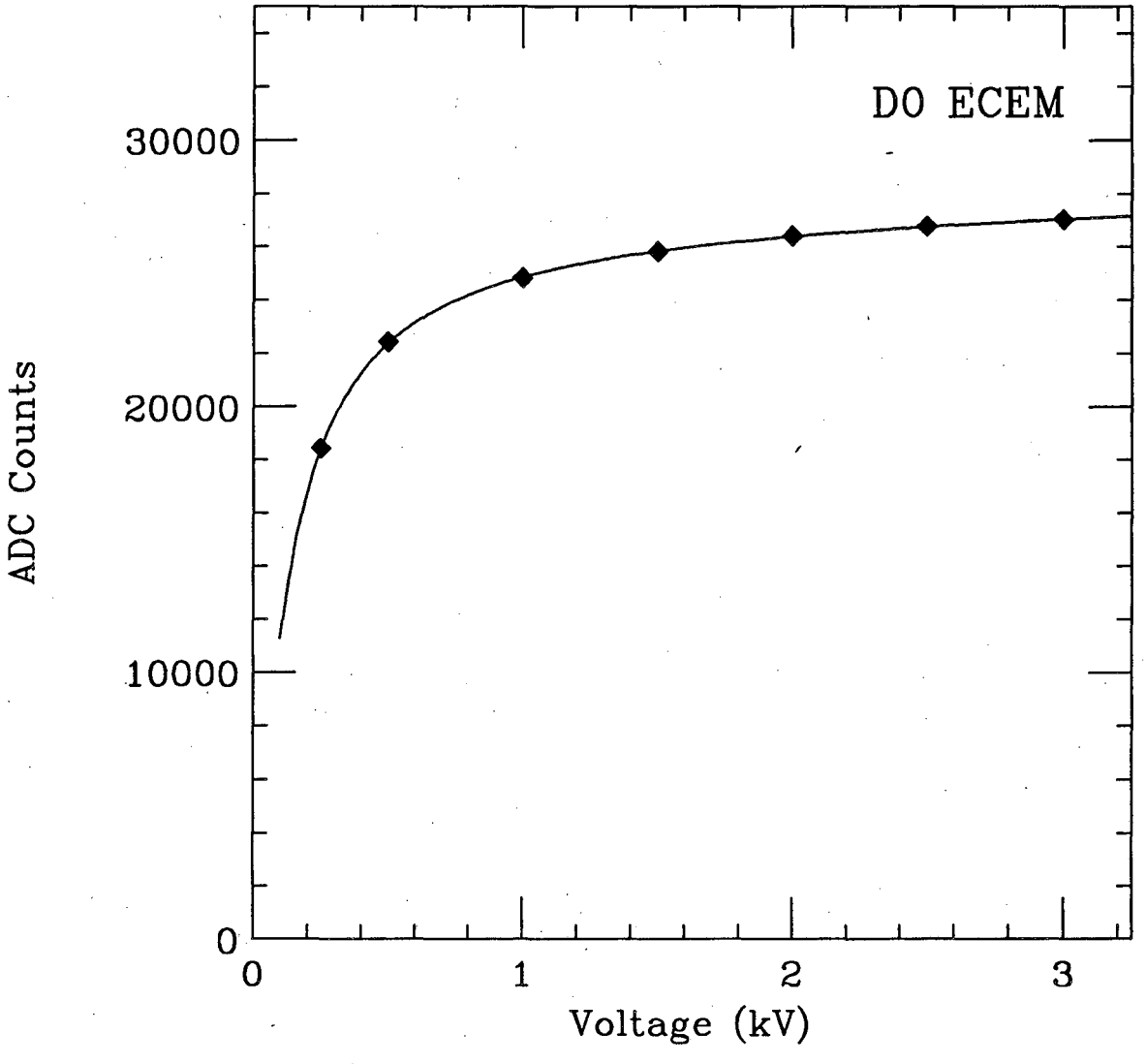

Figure 14: Mean pulse height for 100 GeV electrons at the $\eta = 1.95$ benchmark tower as a function of high voltage.

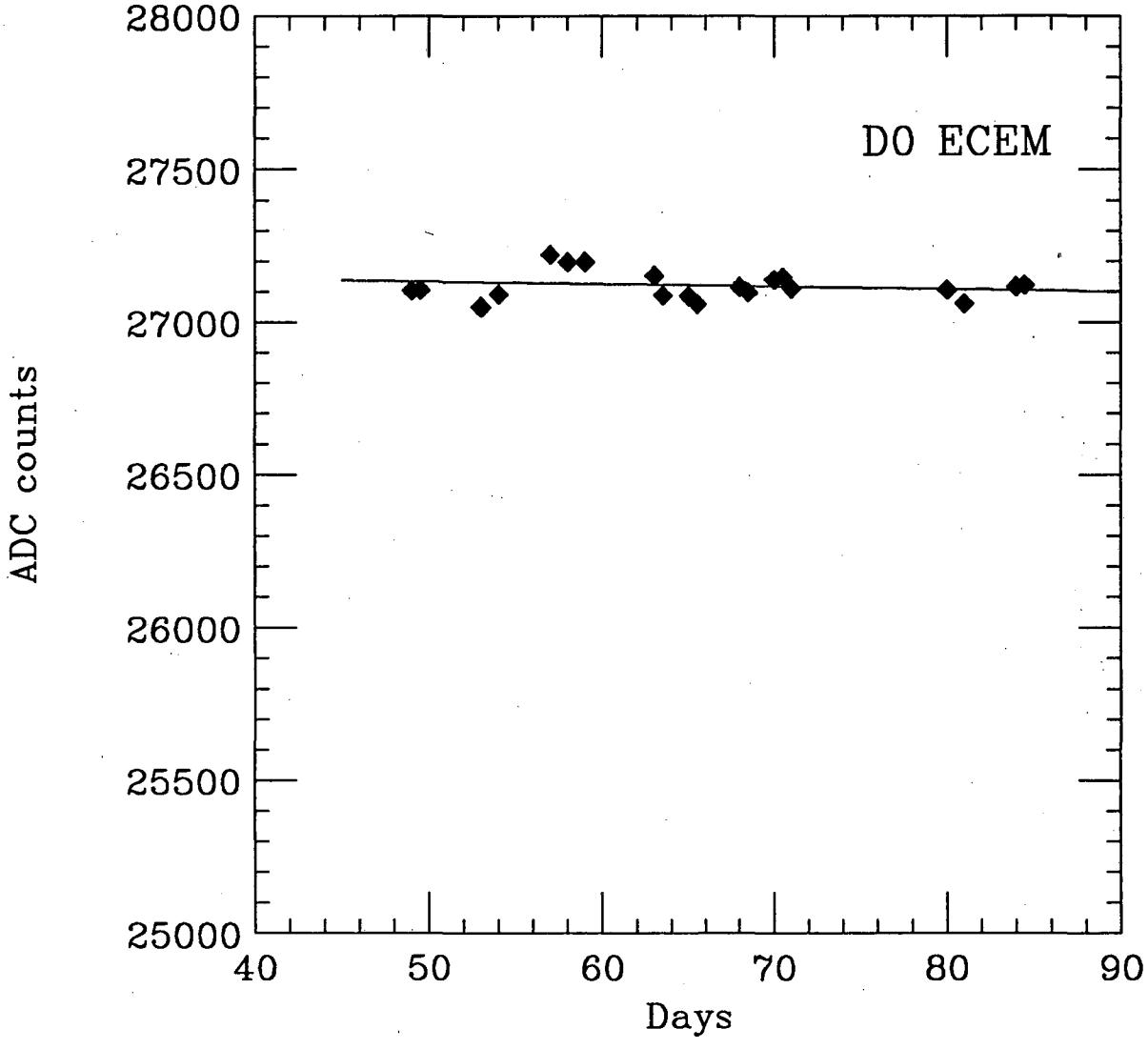

Figure 15: Mean pulse height of 100 GeV electrons at the $\eta = 1.95$ benchmark tower as a function of time during the run. The straight line fit is described in the text.

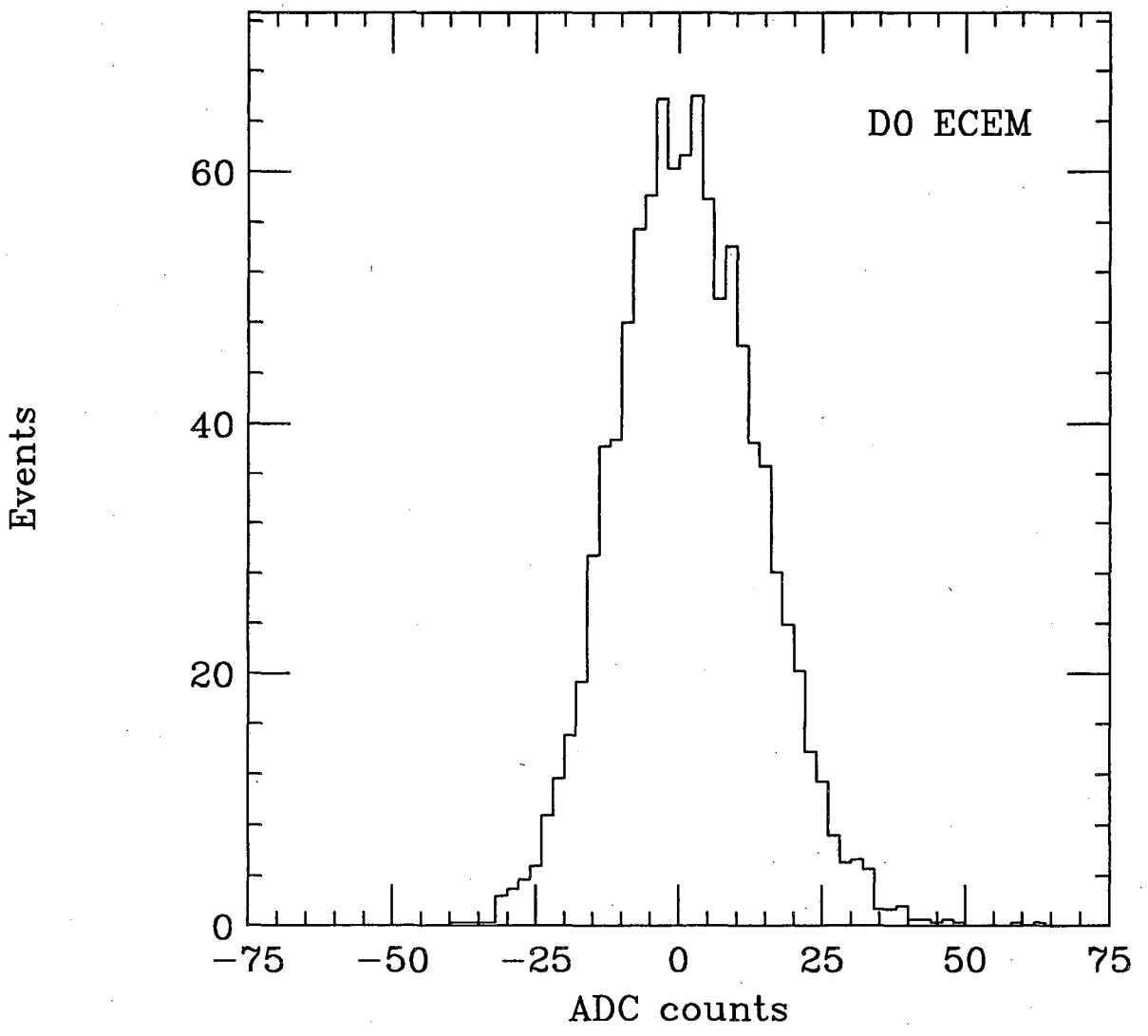

Figure 16: Pedestal distribution in the summed (EM + IH1) benchmark tower ($\eta = 1.95$).

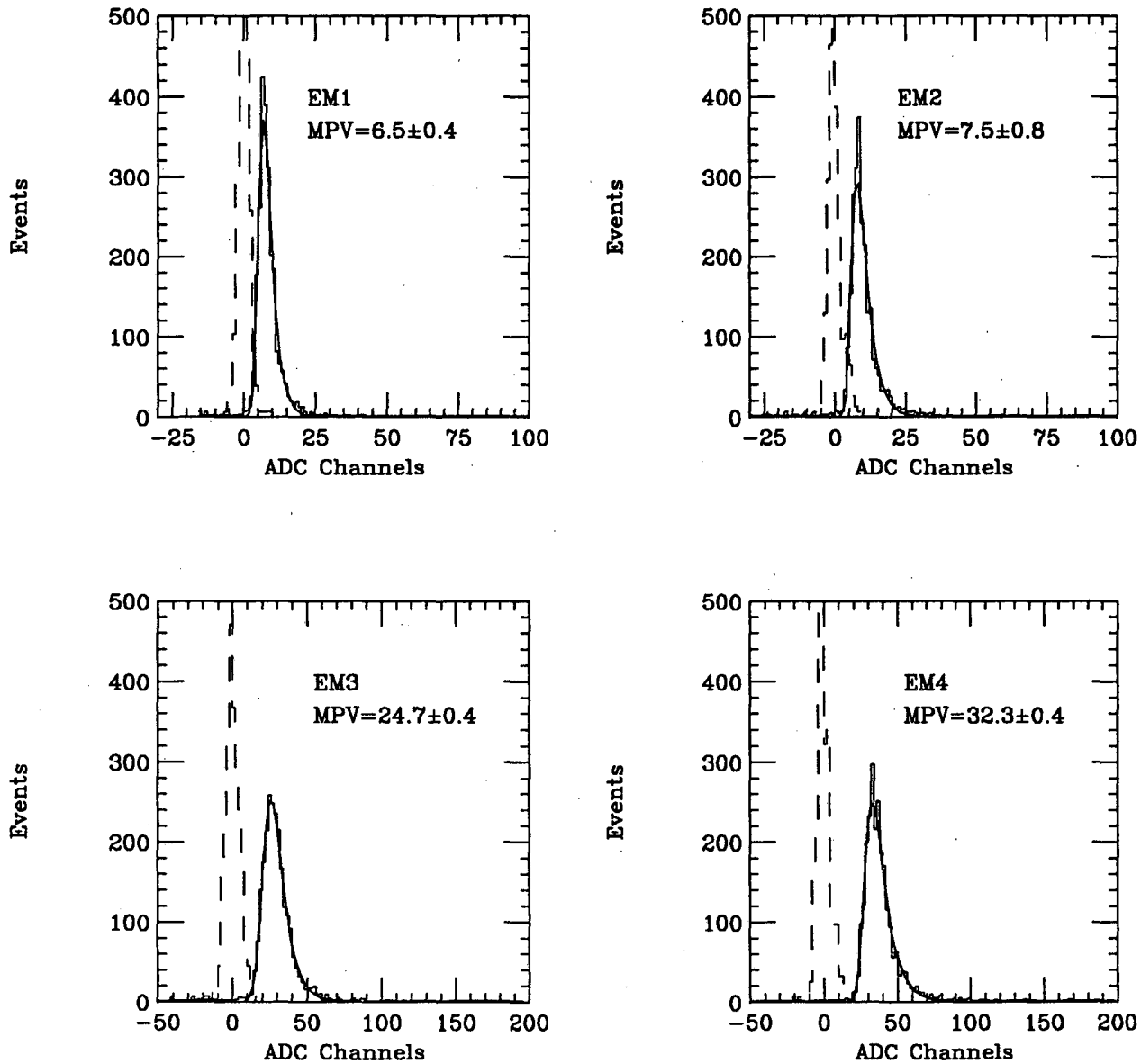

Figure 17: The calorimeter signal in each longitudinal section of the ECEM module for muon triggers (solid histogram) with a fit to a Moyal function (an approximate analytic expression of the Landau distribution) and the pedestal distribution (dashed histogram).

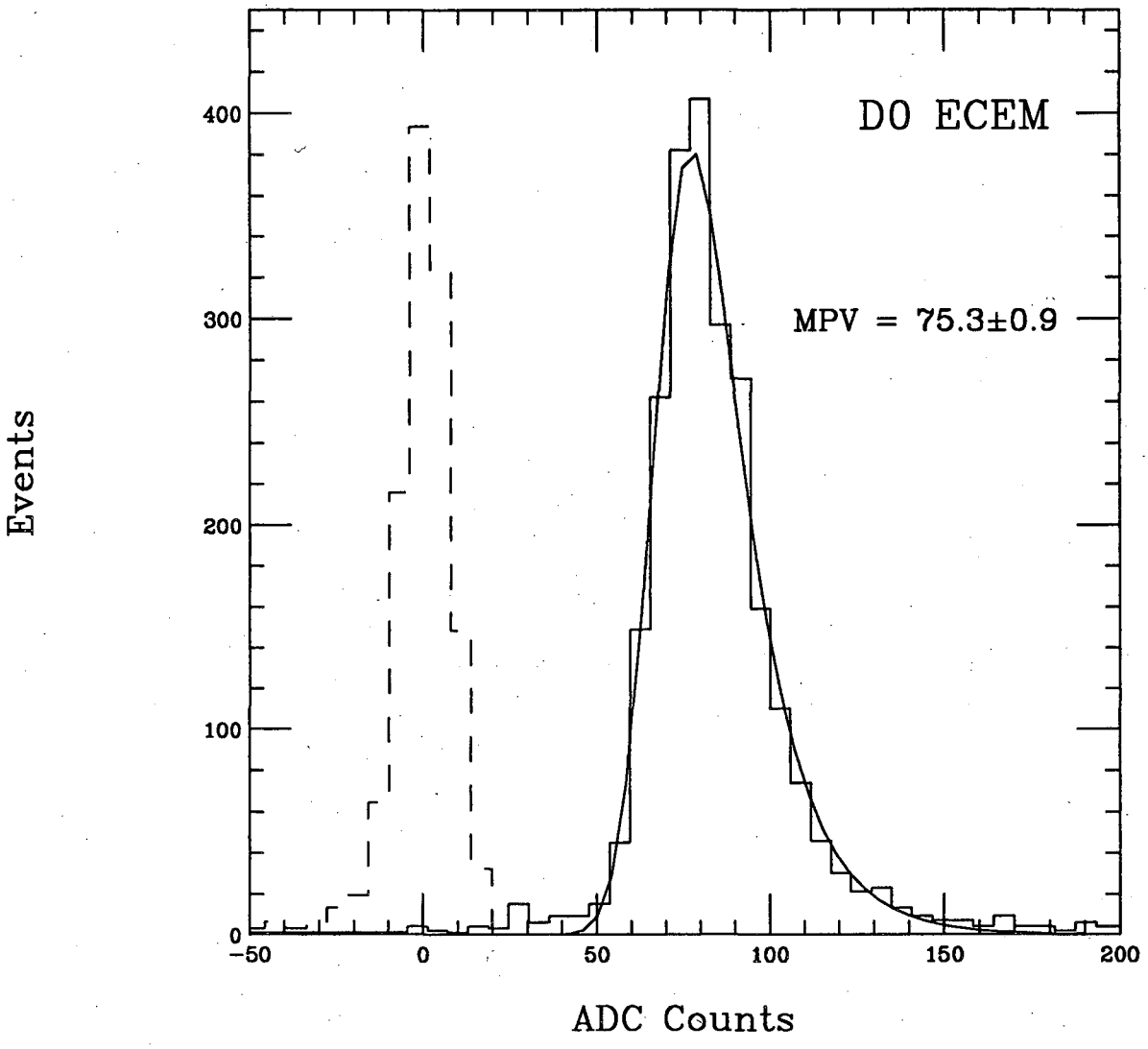

Figure 18: The calorimeter signal summing all four ECEM longitudinal sections for muon triggers (solid histogram) with a fit to a Moyal function (solid line) and the pedestal distribution (dashed histogram).

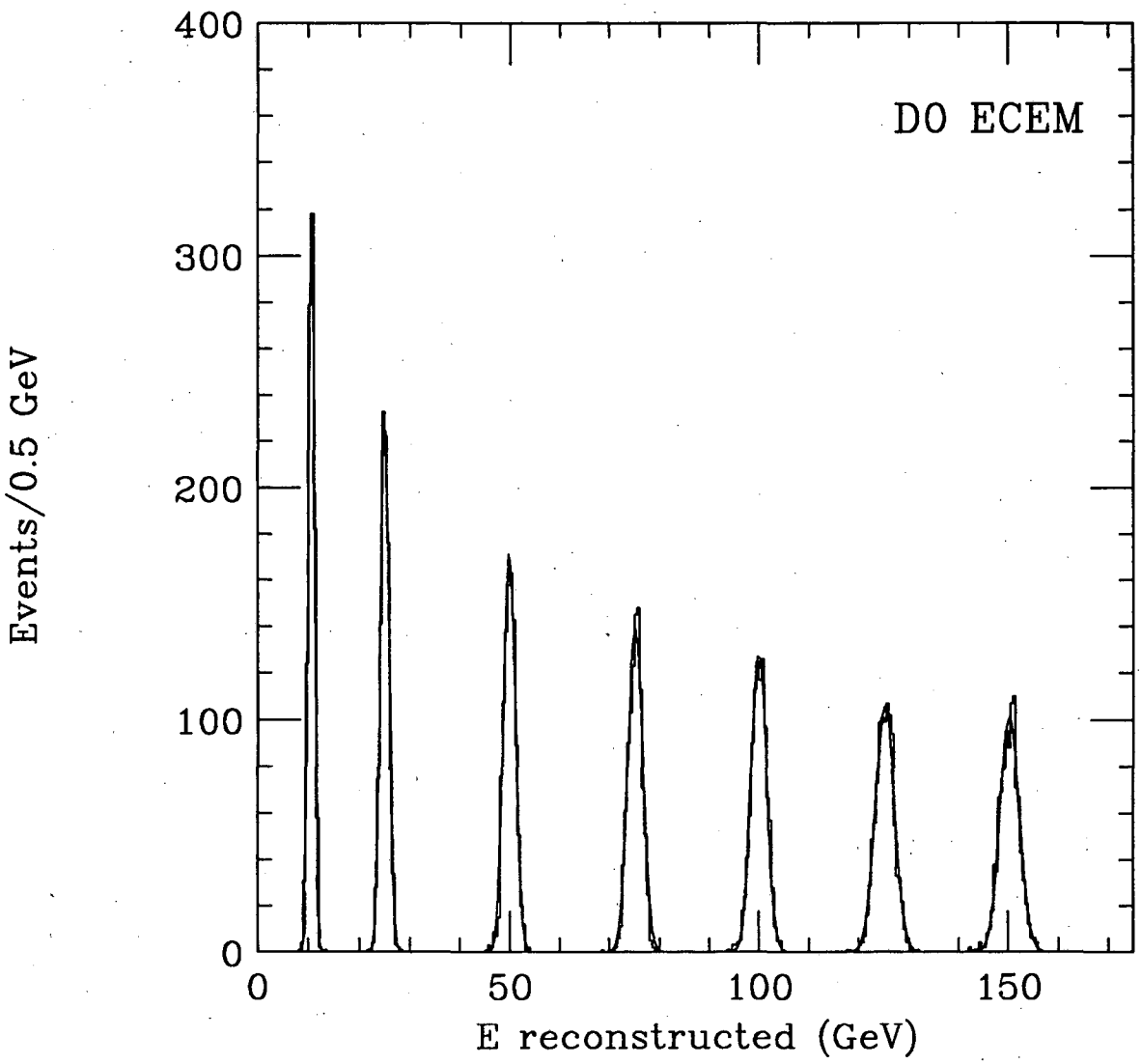

Figure 19: Energy spectra measured in the calorimeter for runs with electron beams with momentum of 10, 25, 50, 75, 100, 125, and 150 GeV/c. 1000 events are used for each run.

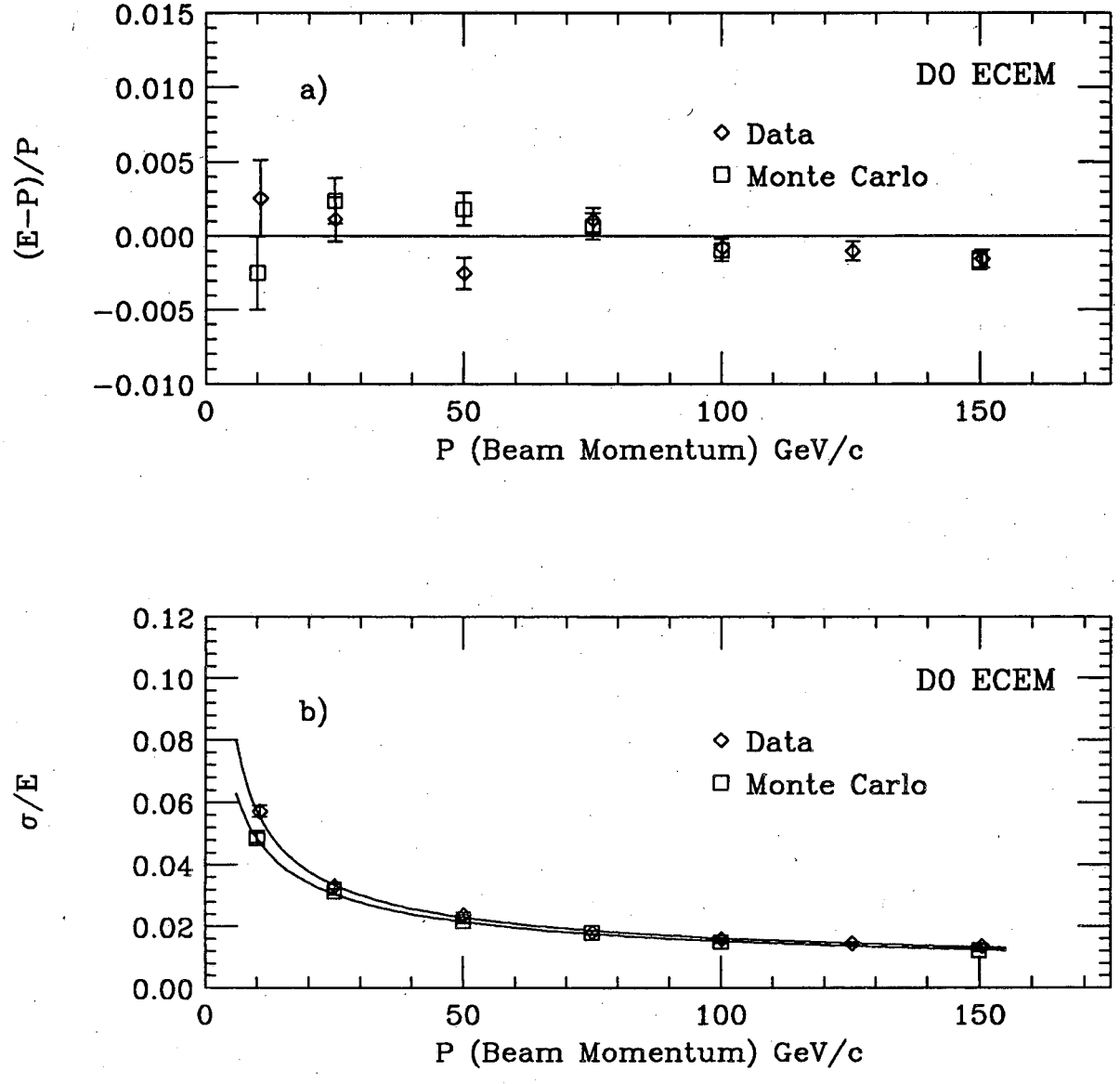

Figure 20: Calorimeter linearity and energy resolution for electrons. a) Fractional deviation of the mean reconstructed energy from the mean track momentum as a function of beam momentum. b) Fractional energy resolution as a function of beam momentum. The fit is the quadratic form (see Eq. 6) and the results are listed in Table 4.

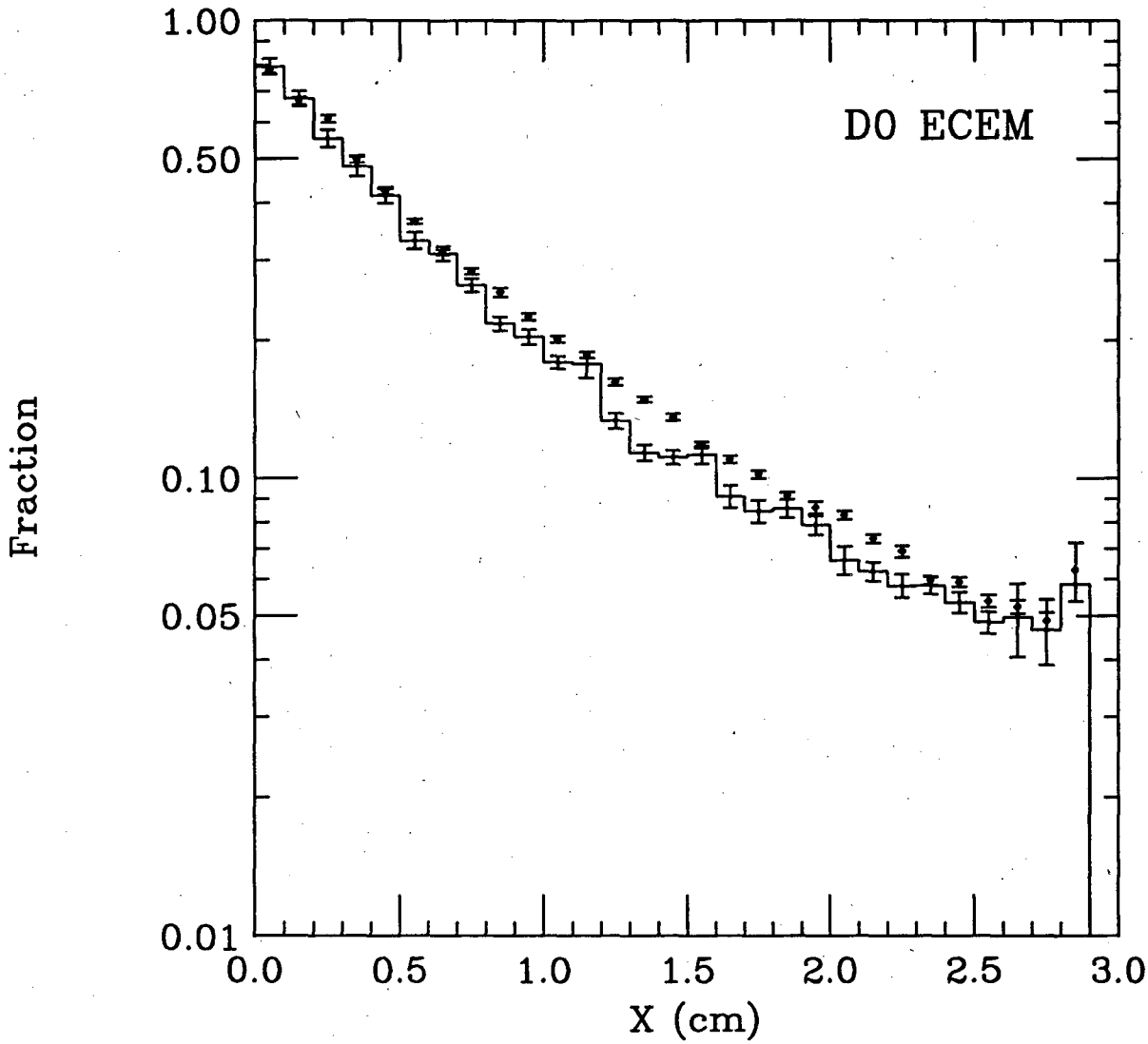

Figure 21: Transverse profile for 50 GeV electron showers in the ECEM. The fraction of energy deposited in all towers a distance $\geq x$ from the shower impact position is plotted vs. x, for data (points) and Monte Carlo (histogram with errors).

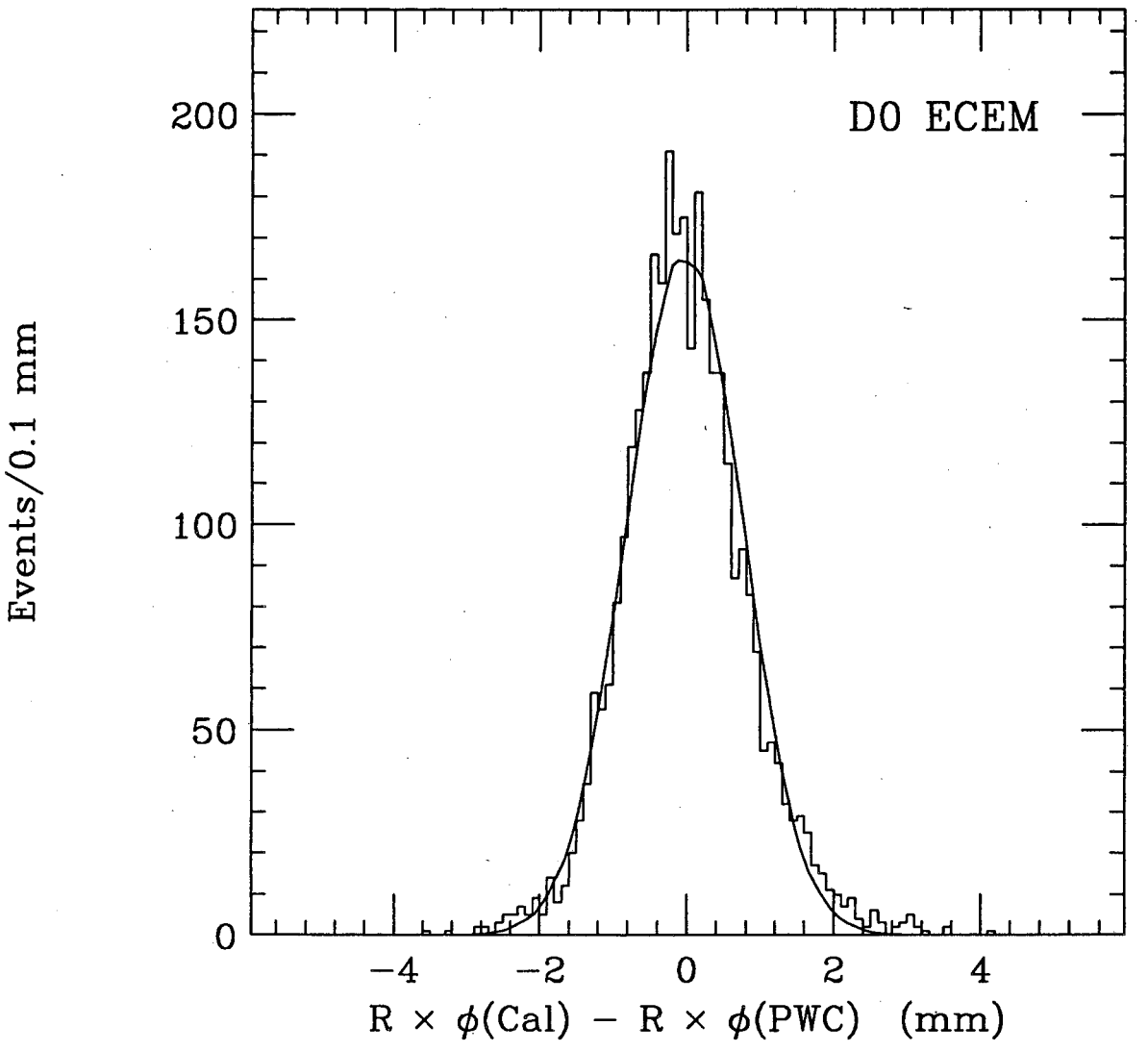

Figure 22: Typical distribution of calorimeter position resolution for an electron run at 100 GeV at $\eta = 1.95$. The curve is a Gaussian fit with mean = $-.034 \pm 0.014$ mm and standard deviation 0.78 ± 0.01 mm.

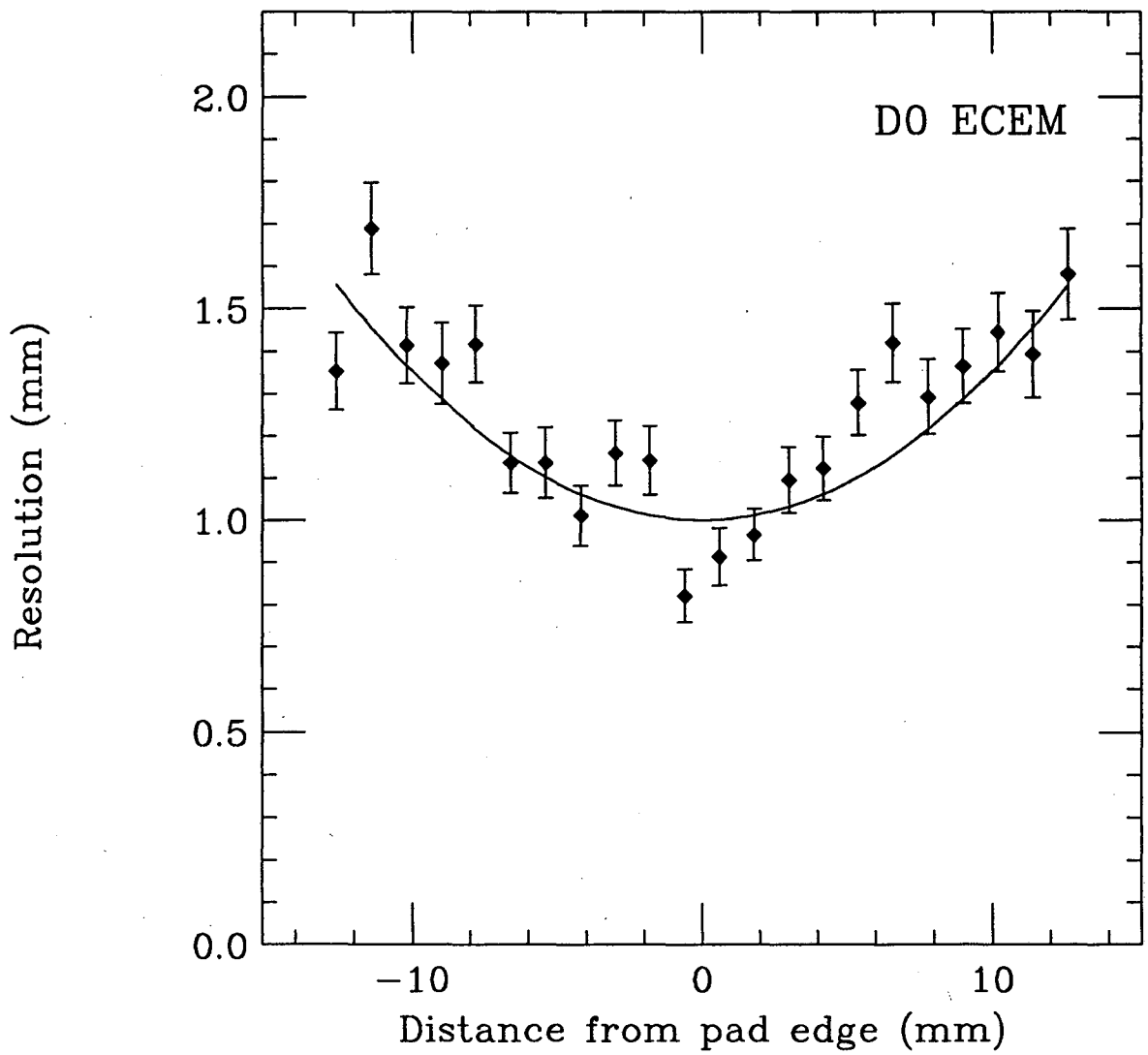

Figure 23: Calorimeter position resolution for 50 GeV electrons as a function of the distance of the shower impact point from the edge of a pad.

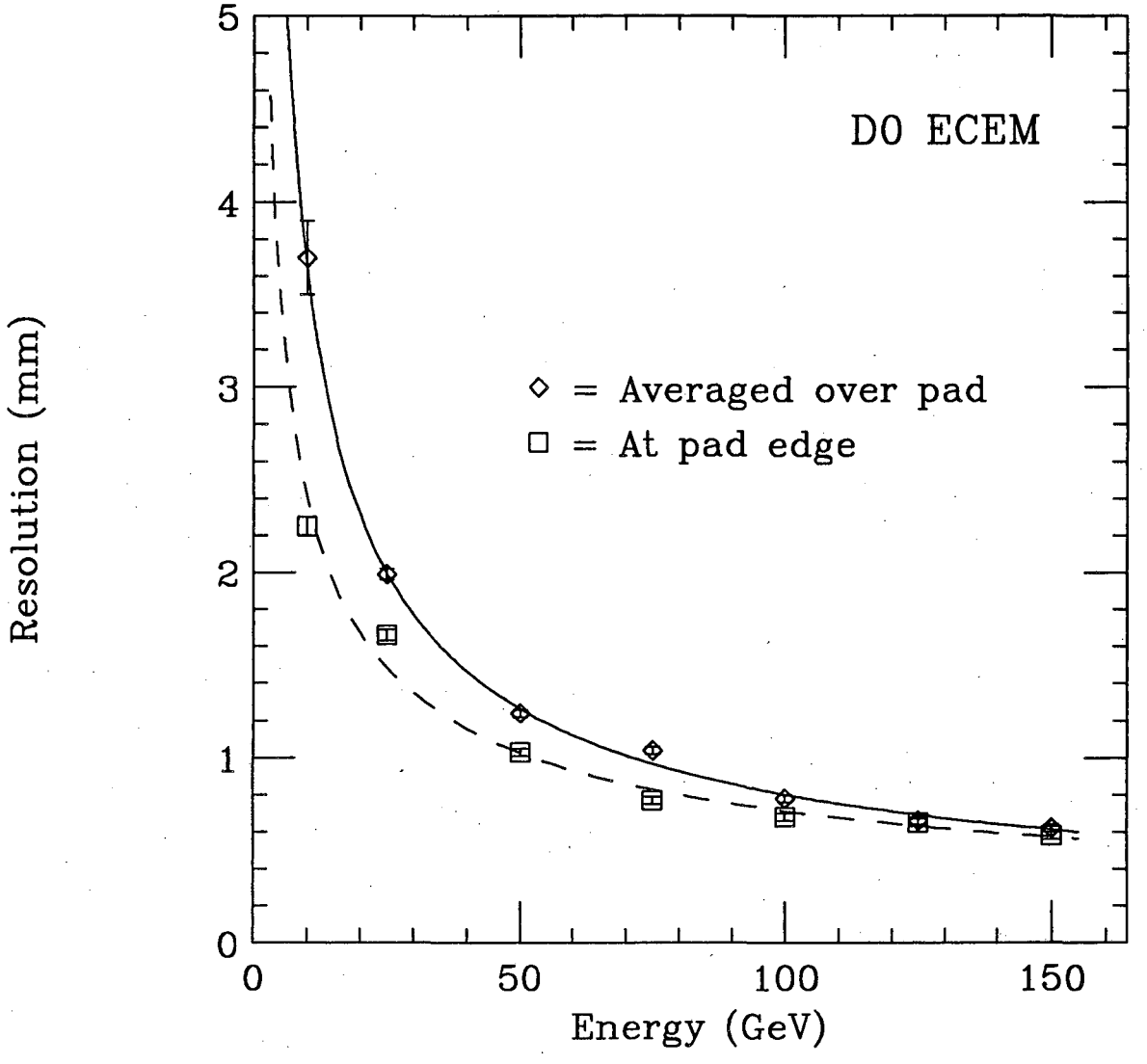

Figure 24: Calorimeter position resolution as a function of the beam energy. The solid line is a fit to the data of the functional form 16.6 mm$\times E^{-0.66}$, and the dashed line is a fit of the form 8.2 mm$\times E^{-0.53}$, where E is the shower energy in GeV.

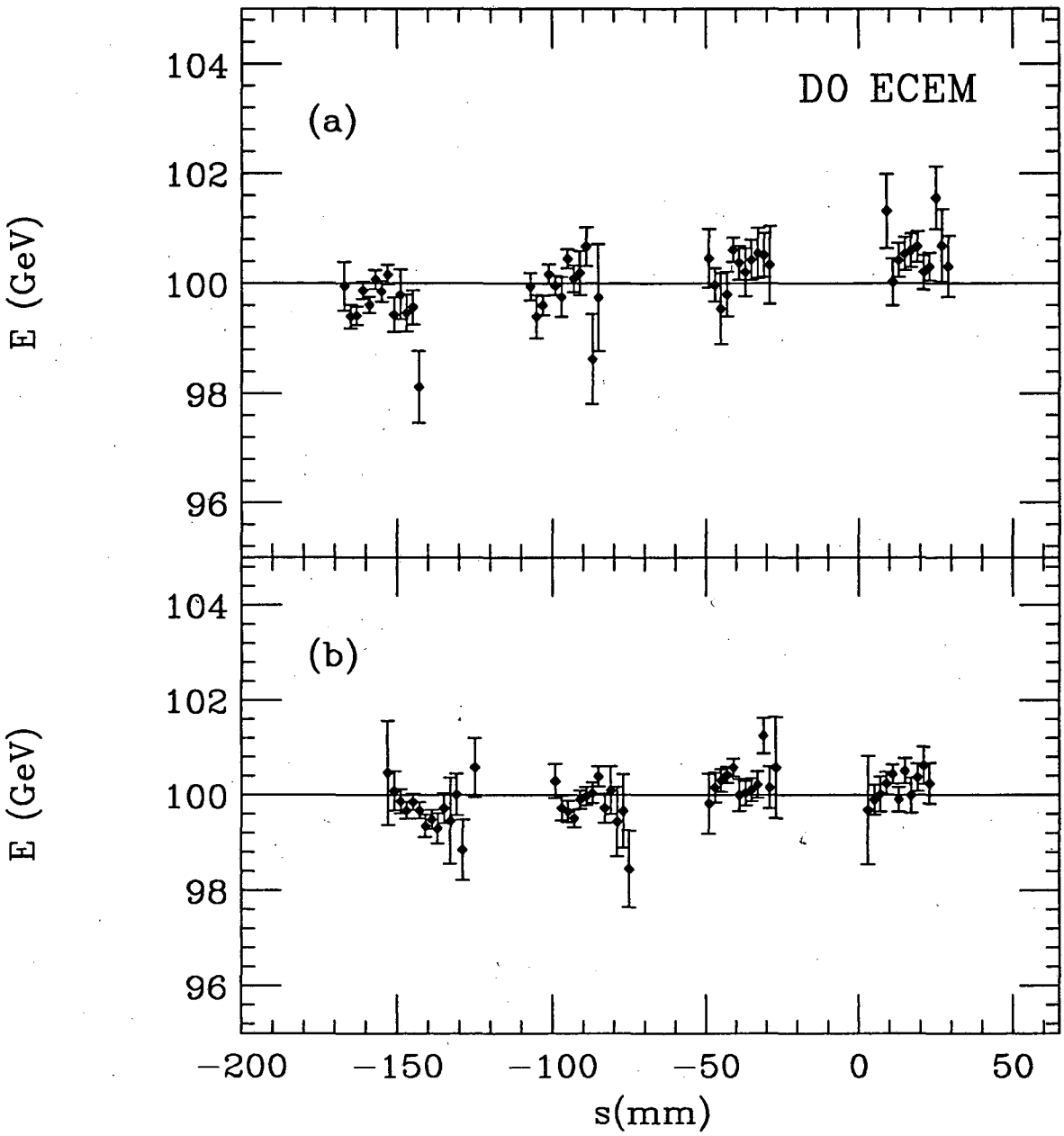

Figure 25: Uniformity of response as a function of azimuth ($s = \mathrm{R} \times \phi$) as determined in runs at η=1.85 (a) and 1.95 (b).

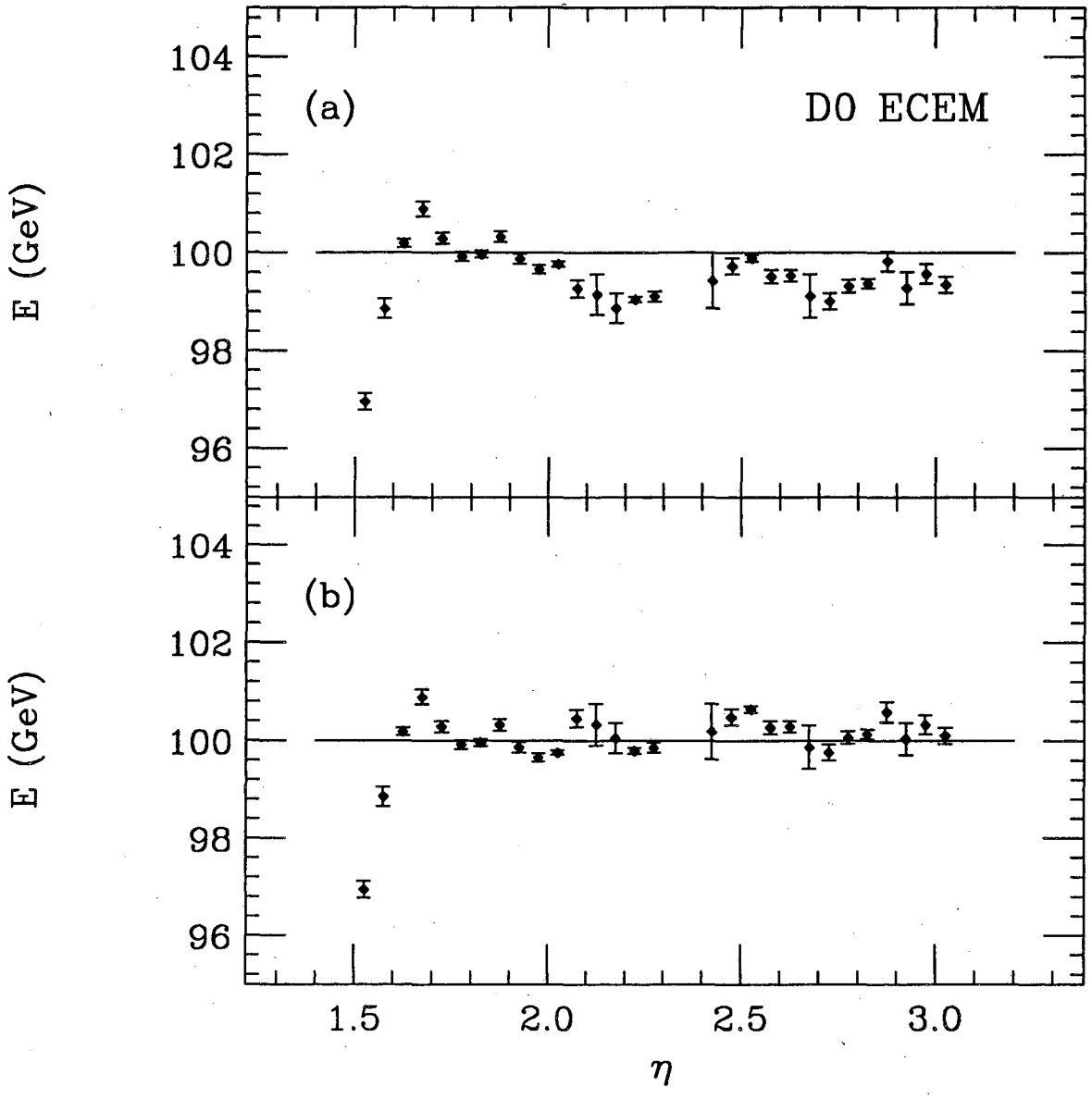

Figure 26: Uniformity of response as a function of η. In (a) the data are analyzed with a single set of parameters. In (b) the data are analyzed using the three sets of parameters listed in Table 5, corresponding to different amounts of material upstream of the ECEM.

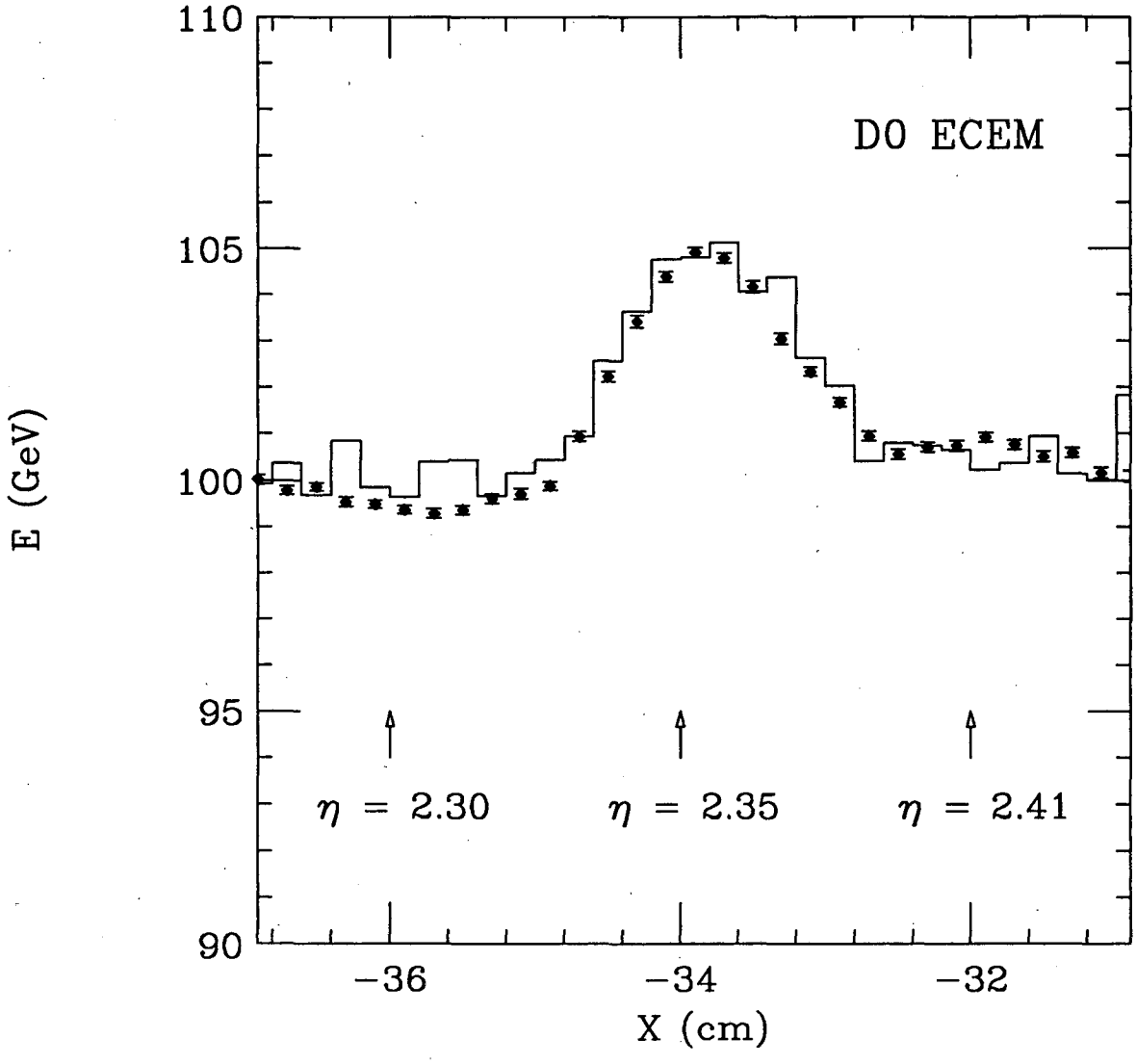

Figure 27: Mean shower energy in the vicinity of the 1 mm gap between uranium plates for 100 GeV electrons as a function of the shower x coordinate in the EM3 layer. The points are the experimental data and the histogram is the result obtained from the Monte Carlo simulation.

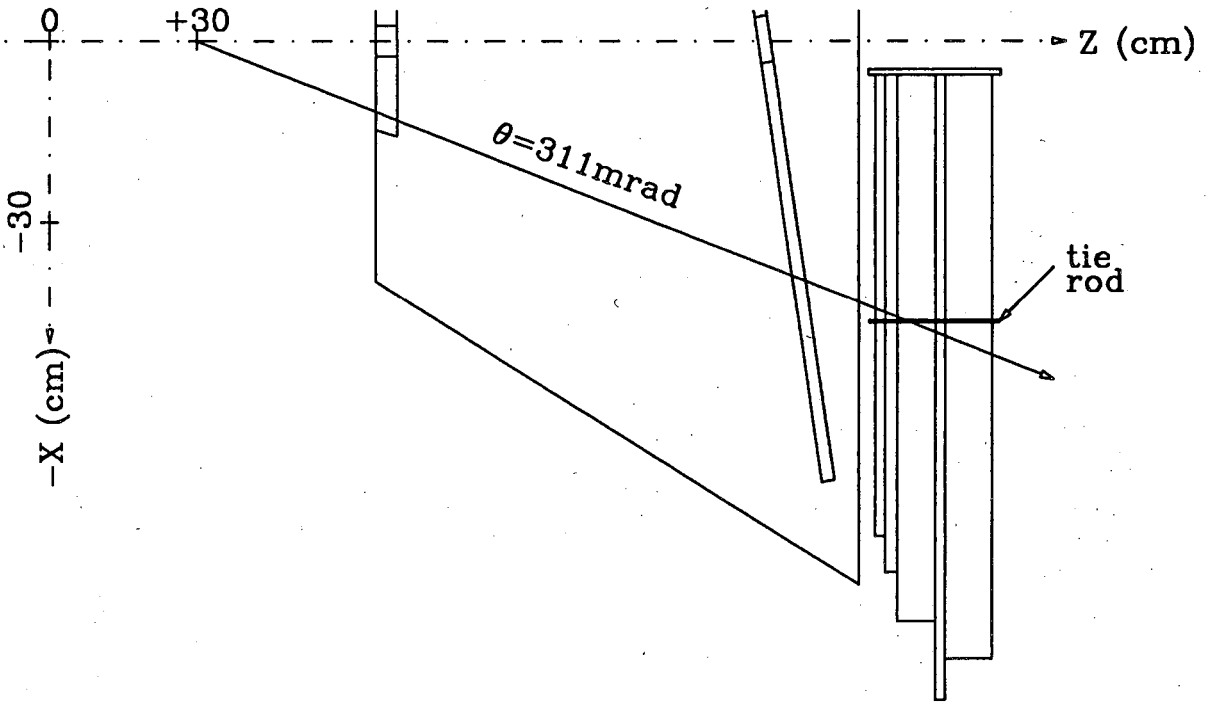

Figure 28: Configuration for the tie-rod studies.

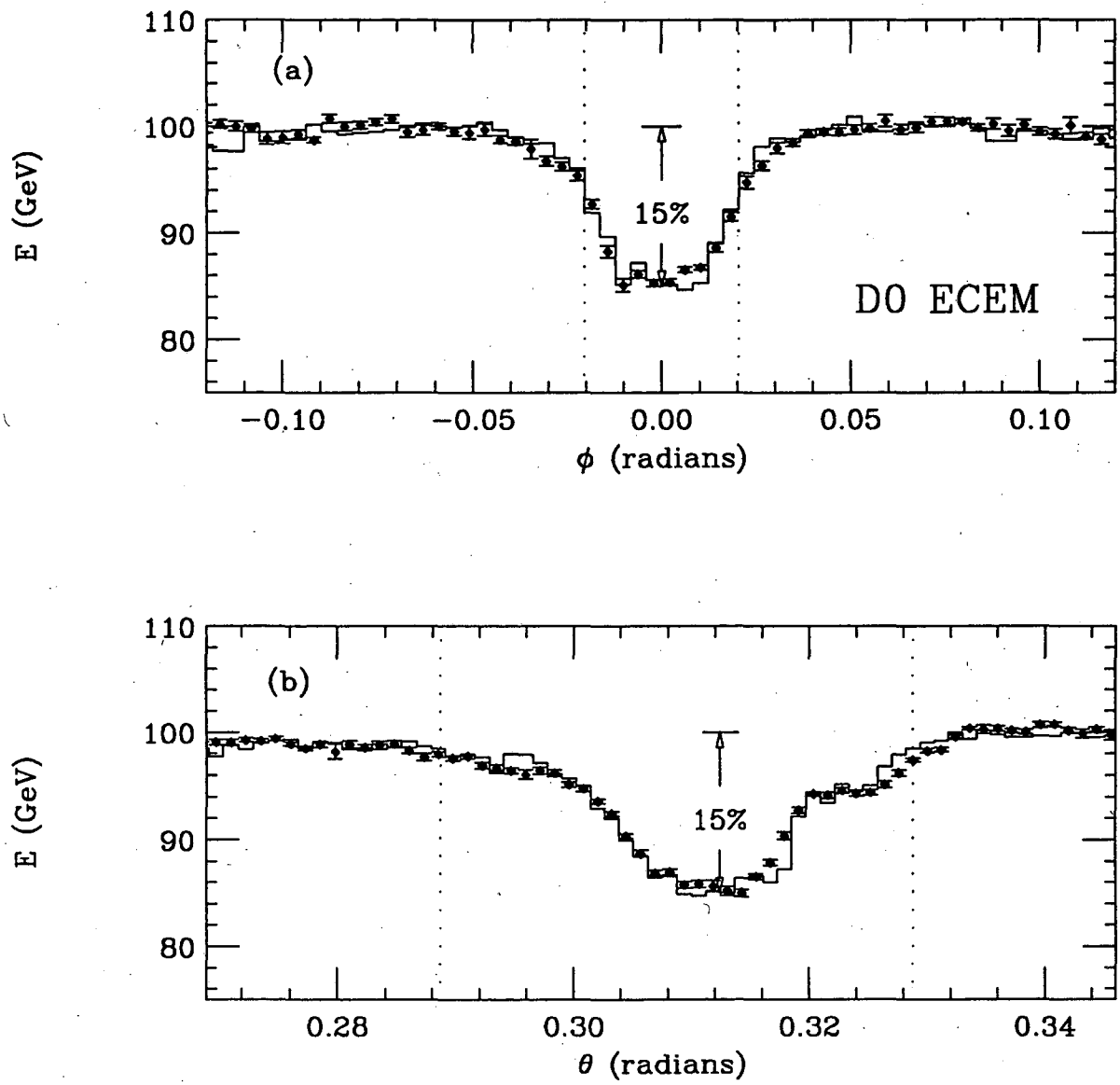

Figure 29: Mean pulse height as a function of azimuth (a), and of polar angle (b) for 100 GeV electrons in the vicinity of the η=2.05 tie-rod. The dotted lines indicate the boundary of the 20 mm diameter zone where the resistive coat has been removed from the signal disks. The points are the data and the histograms are from the Monte Carlo simulation.

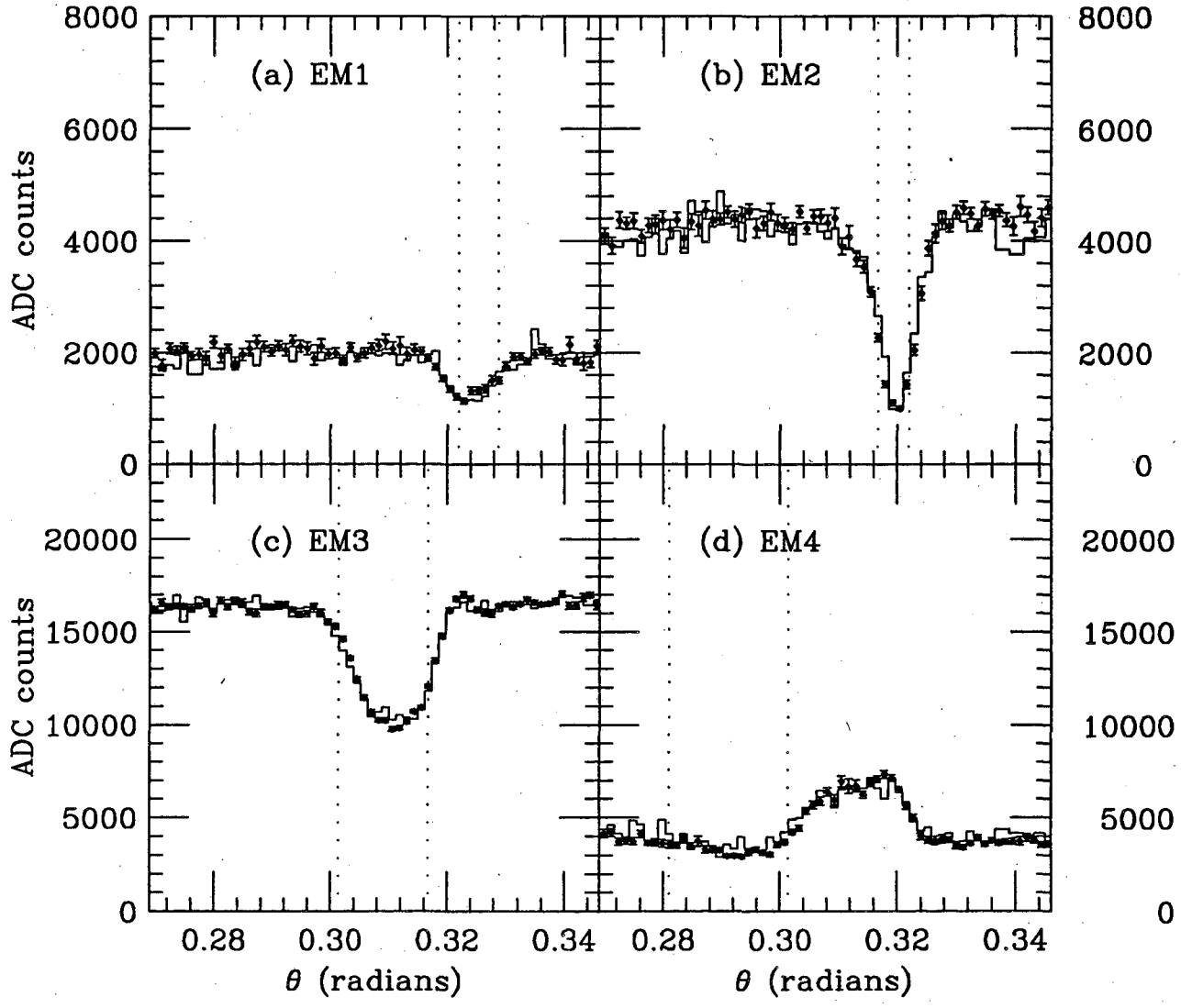

Figure 30: Mean pulse height as a function of the polar angle for EM1 (a), EM2 (b), EM3 (c) and EM4 (d). The dotted lines indicate the boundary within each section of the 20 mm diameter zone where the resistive coat has been removed from the signal disks. The points are the data and the histograms are from the Monte Carlo simulation.

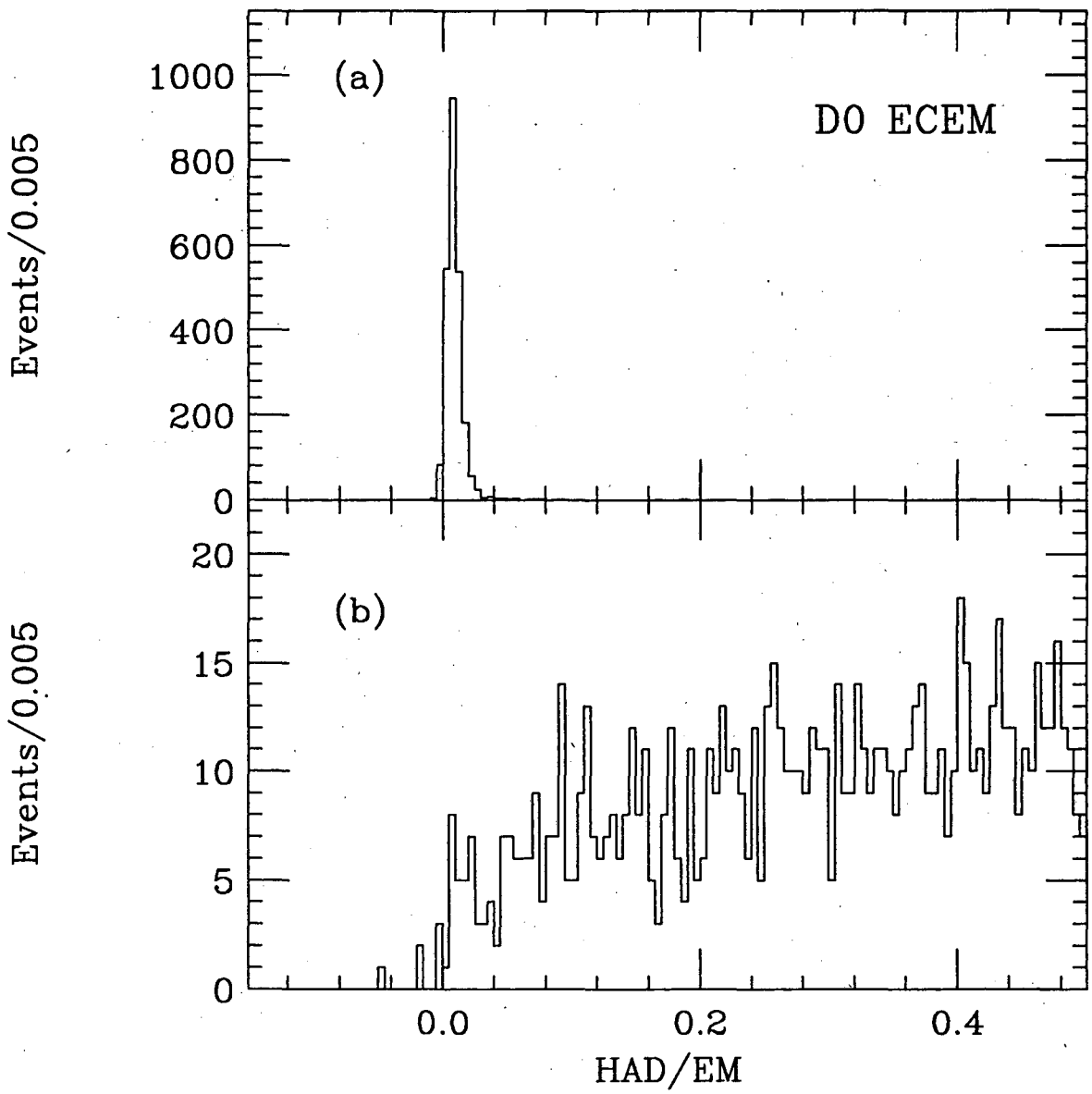

Figure 31: HAD/EM distributions for 2416 electrons (a) and 6517 pions (b) at 100 GeV/c. Only 14% of pions had HAD/EM< 0.5. (The rest of the pions are offscale.)

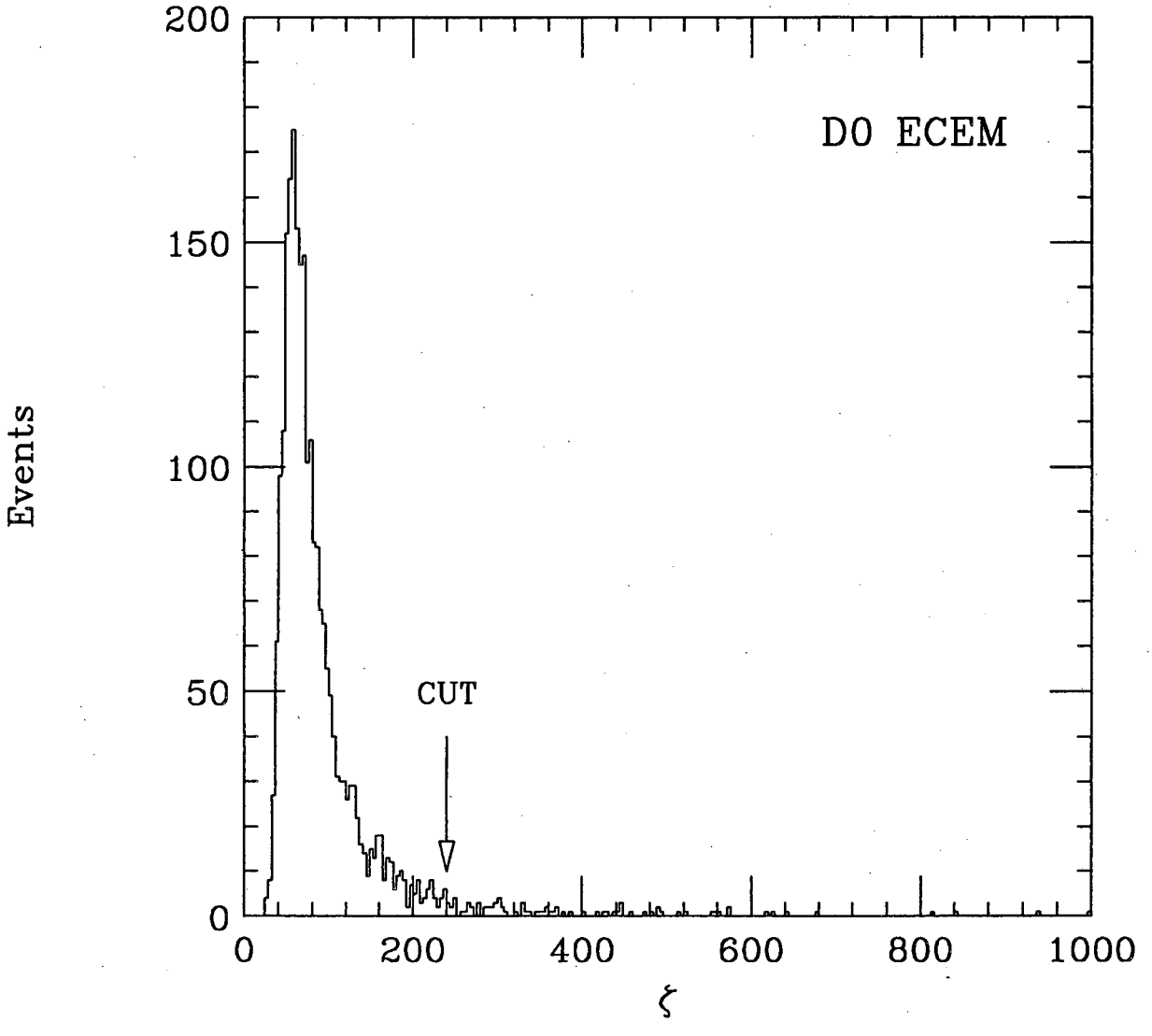

Figure 32: Distribution of the covariance matrix cut variable for 100 GeV electrons.

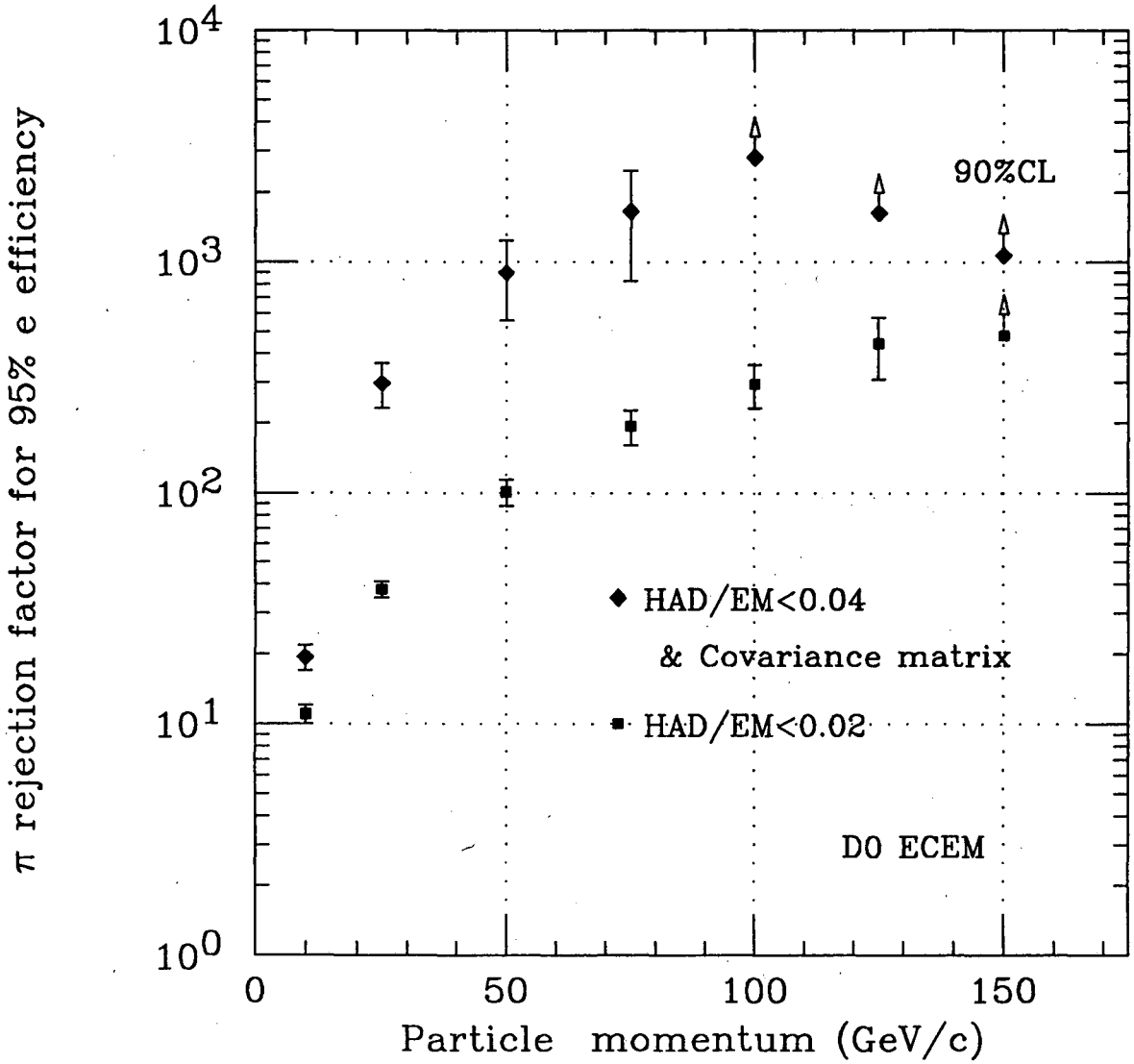

Figure 33: The π rejection factor for 95% electron efficiency as a function of particle momentum (GeV/c).

LAWRENCE BERKELEY LABORATORY
UNIVERSITY OF CALIFORNIA
TECHNICAL INFORMATION DEPARTMENT
BERKELEY, CALIFORNIA 94720